Journal of
Marine Science and Engineering

MDPI

Article

Multiscale Analysis and Prediction of Sea Level in the Northern South China Sea Based on Tide Gauge and Satellite Data

Yilin Yang [1], Qiuming Cheng [2,*], Jin-Yeu Tsou [3], Ka-Po Wong [4], Yanzhuo Men [1] and Yuanzhi Zhang [1,5,*]

[1] School of Marine Sciences, Nanjing University of Information Science and Technology, Nanjing 210044, China; 20201237019@nuist.edu.cn (Y.Y.); 20211237015@nuist.edu.cn (Y.M.)
[2] School of Earth Science and Engineering, Sun Yat-Sen University, Zhuhai 519000, China
[3] Faculty of Engineering, City University of Hong Kong, Hong Kong 999077, China; jytsou@cityu.edu.hk
[4] Department of Applied Social Sciences, The Hong Kong Polytechnic University, Hong Kong 999077, China; portia.wong@polyu.edu.hk
[5] Department of Geography and Resource Management, Faculty of Social Science, Chinese University of Hong Kong, Hong Kong 999777, China
* Correspondence: qiuming.cheng@iugs.org (Q.C.); yzhang209@nuist.edu.cn (Y.Z.); Tel.: +86-188-8885-3470 (Y.Z.)

Abstract: Under the influence of global warming, the problem of sea-level rise is becoming increasingly prominent. The northern part of the South China Sea (SCS) is low lying, with intense economic development, and densely populated. These characteristics make the region extremely sensitive to the consequences of rising sea levels. This study aims to reveal the trends of sea-level changes in the northern SCS and provide scientific insights into the potential flooding risks in low-lying areas. To achieve this, the Ensemble Empirical Mode Decomposition (EEMD) method is used to analyze the water level time series data from three tide gauges along the coast of Hong Kong. This analysis reveals the multidimensional change characteristics and response mechanisms of the sea level in the SCS. The findings reveal distinct seasonal, interannual, decadal, and interdecadal variations in sea-level changes. Furthermore, we explore the impact of the El Niño-Southern Oscillation (ENSO) on sea-level changes in the study area, finding a 6-month lagged correlation between the sea level and ENSO. Spatially, the rate of sea-level change is faster in nearshore areas than in the open ocean and higher in the northern regions than in the southern regions. The Multifractal Detrended Fluctuation Analysis (MF-DFA) method is employed to analyze the sea-level change time series, revealing long-range correlations and multifractal characteristics. In addition, we propose a sea-level prediction method that combines EEMD with Long Short-Term Memory (LSTM) neural networks and conducts empirical research on sea-level changes in the northern South China Sea. The results indicate that the EEMD-LSTM model outperforms the standalone LSTM model in terms of predictive accuracy, effectively eliminating noise from signals and providing a valuable reference. In summary, this research delves into the multiscale characteristics and influencing factors of sea-level changes in the northern SCS, proposing an improved sea-level prediction method that integrates EEMD and LSTM. The findings lay the groundwork for evaluating the risks of sea-level rise in low-lying regions of the northern SCS and inform future response strategies.

Keywords: sea-level change; Northern South China Sea; multiscale analysis; tide gauge data; sea-level prediction

check for updates

Citation: Yang, Y.; Cheng, Q.; Tsou, J.-Y.; Wong, K.-P.; Men, Y.; Zhang, Y. Multiscale Analysis and Prediction of Sea Level in the Northern South China Sea Based on Tide Gauge and Satellite Data. *J. Mar. Sci. Eng.* **2023**, *11*, 1203. https://doi.org/10.3390/jmse11061203

Academic Editor: Chung-yen Kuo

Received: 8 May 2023
Revised: 27 May 2023
Accepted: 4 June 2023
Published: 9 June 2023

1. Introduction

Globally, climate warming has become an increasingly severe issue, accompanied by the ever-growing concern of sea-level rise. Since 1900, the global mean sea level has been rising at a rate of 1.77 ± 0.38 mm per year, with the rate of global sea-level rise in the 21st century having surpassed the average level of the 20th century [1–3]. The Sixth Assessment Report on climate change released by the Intergovernmental Panel on

Climate Change (IPCC) emphasizes that the changes in the climate system over the past several centuries, or even millennia, have been unprecedented [4]. Coastal areas, which are typically characterized by significant economic importance, have become increasingly vulnerable to global sea-level rise. In particular, low-lying coastal areas are increasingly facing the risk of land inundation and ever-more-frequent extreme disaster events [5–9]. At the regional level, sea-level changes often exhibit entirely different patterns from global sea-level rise, potentially deviating significantly from the global averages. The underlying causes are related to changes in ocean circulation dynamics and the equilibrium adjustment of the Earth's crust [10]. On a regional scale, the rate at which the sea levels in the South China Sea (SCS) are rising is much higher than the global average rate [11,12]. Notably, the growth rate of sea-level rise of coastal land areas in southern China is also faster than the global average [13,14].

From 1993 to 2019, although the global average rate of sea-level rise was at 3.2 mm/year, due to the influence of hydrometeorological conditions, runoff into the ocean, and vertical ground motion, regional differences in global sea-level changes were evident [15–19]. For example, between 1980 and 2020, China's coastal sea level demonstrated an accelerated upward trend, and compared to the global annual average for sea-level rise of 3.3 mm/year from 1993 to 2020, China's coastal sea level rose at a rate of 3.9 mm/year in the same period [20]. Current regional sea-level changes appear to be primarily driven by natural climate variations, with coastal sea-level changes in the past 60 years predominantly governed by the ocean circulation [21,22]. The influence of human activities on regional sea levels will gradually deepen as climate change progresses, and by the end of the 21st century, regional sea-level patterns will be a superposition of climate change patterns and static sea-level patterns resulting from the combined effects of natural and anthropogenic factors [23,24].

The existence of tide gauges provides data support for the study of long-term changes in sea level [25,26]. By necessity, tide gauge stations are located in coastal areas. Along these lines, early research on sea-level changes in the northern SCS was mostly limited to the coast of Guangdong. Early studies highlighted the rising sea level in the waters near Hong Kong, which rose at a rate of 1.9 ± 0.4 mm/year from 1954 to 1999. In contrast, the sea level of the waters near Macau rose at an average rate of about 1.35 mm/year from 1925 to 1970, but then jumped to about 4.2 mm/year from 1970 to 2010 [14,27].

Meanwhile, satellite altimeter technology offers certain advantages, including global coverage and timing sampling, which can effectively compensate for the sparse observation of tide gauges. Therefore, since the 1990s, satellite altimetry has become the primary tool for sea-level data collection [28,29]. In the early days of 1990s, due to the limitation of the measurement cycle, most of the research examining sea levels in the SCS focused on the annual change data. More recently, various scholars have analyzed Topex/Poseidon data, uncovering significant interannual changes in sea levels in this region. Specifically, in the winter months, the sea level above the entire deep-sea basin is low, with two low centers, one near Luzon and the other on the Sunda continental shelf. Meanwhile, the summertime is dominated by the southwest monsoon phenomenon; consequently, the sea levels near Luzon Island and the Sunda Shelf are high, while a low area near Vietnam separates the two [30]. As altimeter measurement has increased over time, new research has focused on the interannual and long-term changes to sea levels in the SCS [11,12,31].

Although the sea level in the SCS has demonstrated the trend of a rapid rise on an extended time scale, some studies have clarified that the sea-level change in the SCS is actually fluctuating, even showing a sharp decline in some years. For example, Cheng and Qi [11] investigation of changes in sea level in the SCS revealed that sea levels followed an upward trend from 1993 to 2000, with a rising rate of 11.30 mm/year. This period was followed by a fluctuating decline from 2001 to 2005, with a decline rate of 11.80 mm/year. Scholars have advanced various explanations for such changeable data. For example, as a result of Vivier, et al. [32] examination of the causes of sea-level changes in the SCS, the researchers concluded that baroclinic Rossby waves, specific volume, and wind stress forces are the main factors affecting sea-level height changes in the region.

According to Fang, et al. [12], the sea level of the SCS rose by 6.7 ± 2.7 cm/decade from 1993 to 2003; the authors also uncovered a certain correlation between the phenomenon and El Niño and Southern Oscillation (ENSO) on the intradecadal scale. Other researchers have also asserted that ENSO can affect the sea-level height of the SCS through the influence of the SCS monsoon and the North Pacific circulation (Kuroshio). In particular, the sea level of the whole ocean decreases synchronously during El Niño and rises during La Niña cycles [33–35]. Other researchers who conducted spectral analysis of the global average sea-level change rate identified a 4 to 8 year fluctuation period, which is close to the frequency of ENSO, thus largely reflecting the impact of El Niño on sea-level changes [36].

The sea-level time series signal is nonlinear and nonstationary, it has a fluctuation trend especially under the influence of El Niño, typhoon, human land reclamation, etc. In recent years, many scholars have used a variety of methods to analyze the multiscale changes in sea level [26,37]. One such method is empirical mode decomposition (EMD), used for processing nonlinear and nonstationary signals. Because of its achievement, this technique is currently widely used in atmospheric and marine research [38]. Another method, ensemble empirical mode decomposition (EEMD), was developed from EMD. This newer approach involves adding one or more groups of white noise signals on the basis of EMD to stabilize the original time series data [39]. Researchers have sought to obtain the spatiotemporal variation trend of sea level by applying the EEMD method to the study of multiscale spatial–temporal variation of sea level in recent years [40–42]. For example, Kim and Cho [43] used EEMD to analyze data from tide gauge stations around the Korean Peninsula to determine the trend of sea-level change and facilitate predicting it. Along similar lines, Lan, et al. [44] used the EEMD method with tide gauge data to study the trends, characteristics, and related mechanisms of annual sea-level amplitude in the North Pacific. According to their results, the annual amplitude decline of the west coast of the SCS has been quite consistent with the annual average wind stress related to the Pacific Decadal Oscillation (PDO).

In addition, detrended fluctuation analysis (DFA) has proved to be one of the most widely used and reliable tools for detecting the long-term correlation of nonstationary time series and has been successfully applied to life sciences, meteorology, and other fields [45]. Basing their efforts on DFA, Kantelhardt, et al. [46] proposed further multifractal detrended fluctuation analysis (MF-DFA) of unstable finite series. This approach is useful for detecting the long-range correlations and determining scale invariance, as well as judging whether a sequence has multifractal properties [47–49]. Zhou and Leung [50] calculated the long-range correlation of sunspot time series based on this method. Meanwhile, Zhang and Ge [51] used multifractal temporal weighted DFA to analyze the long-term correlation and multiscale behavior of sea-level rise in Hong Kong. The researchers demonstrated that sea-level rise had multifractal characteristics and spatial heterogeneity. Ye, et al. [52] applied MF-DFA to study the complexity of the daily runoff fluctuation in the variegated Lake Basin of Poyang Lake Basin in China, finding that the multifractal of the runoff fluctuation had significant regional characteristics.

Although significant progress has been made in the research and methodologies of sea-level change, the long-term trends and uncertainties of sea-level changes pose challenges to prediction, as the results may be influenced by various factors. Over the past several decades, methods and techniques for predicting sea-level changes have been continuously evolving and improving. Early prediction approaches primarily relied upon empirical equations and statistical models. In recent years, with the advancement of technology and the increasing availability of data sources, new prediction methods and models have emerged. Currently, commonly used methods for predicting sea-level changes include physical models, statistical models, and machine learning techniques [53–55]. Among these, physical models are mathematical models established based on physical principles that account for various complex atmospheric and oceanic environmental factors, such as ocean circulation, wind, tides, and seafloor topography, and therefore exhibit higher accuracy and reliability [56]. However, the development of physical models necessitates extensive data and complex calculations, leading to high computational costs and requiring accurate understanding and assessment of the impacts of various influencing factors. Neural network predictions, particularly the advent of deep learning technology, have experienced rapid growth in recent years and have further improved the prediction accuracy. Unlike traditional statistical models, deep learning does not require making any assumptions about factors; instead, it enables algorithms to autonomously explore the patterns and features within data [57]. Qu, et al. [58] discovered that under two different temperature elevation thresholds, sea-level rise is primarily influenced by volumetric expansion, while the impact of local land movement on predictions is relatively minor.

The application of LSTM neural networks in the field of Earth sciences is also increasingly widespread [59,60]. It is also used in the processing and prediction of sea-level height time series [61]. Zhao, et al. [62] utilize China's first global ocean Climate Data Records to analyze and predict sea-level changes in the Yellow Sea, employing a novel SSA-LSTM combined model for improved accuracy. The research highlights the strong relationship between sea-level trends, seasons, and latitudes, while projecting a continued rise rate of 3.65 ± 0.79 mm/year for the next decade. Given that sea-level changes are affected by various factors, it is imperative to develop efficient prediction models to better understand their patterns of change and make effective predictions.

Sea-level fluctuations exhibit intricate scale-dependent behavior, characterized by considerable spatiotemporal variations and spatial heterogeneity. Investigating regional sea-level changes, as different from global trends, allows for a more direct assessment of the potential impacts on local economies and ecological environments. Consequently, examining the alterations and attributes of sea levels in the northern SCS bears practical significance. Previous research within the SCS predominantly focused on the velocity and driving forces of sea-level rise on extended timescales. The present study endeavors to examine the multiscale and multifractal features of sea-level changes in the northern SCS over the past 20 years, investigate the temporal scale cyclical features and spatial heterogeneity of sea-level changes, and propose an improved sea-level prediction method. By elucidating these properties, this investigation aims to provide valuable scientific evidence for future inundation assessments of coastal cities in the northern SCS.

2. Materials and Methods

2.1. Study Area

As the largest semi-enclosed marginal sea in the Northwest Pacific, the South China Sea (SCS) connects to the East China Sea through the Taiwan Strait, and its eastern part links to the Pacific Ocean through the Luzon Strait. Fresh water from such rivers as the Pearl River and the Han River flows into the Sea from the north. The northern part of the SCS, including the Pearl River Delta, Hong Kong, and Macau Special Economic Zones (i.e., Guangdong–Hong Kong–Macau Greater Bay Area), is one of the most economically developed regions in China. This densely populated region is greatly affected by the monsoon climate, and the sea conditions in the adjacent offshore areas have a significant impact on coastal regions.

2.2. Datasets

The Hong Kong Observatory (HKO) manages six tide gauges, Quarry Bay (QUB), Shek Pik (SPW), Tai Miu Wan (TMW), Tai Po Kau (TPK), Tsim Bei Tsui (TBT), and Waglan Island (WAG), which record hourly sea-level changes in the Hong Kong Sea area. The HKO's tide gauge station is a high-precision ocean monitoring system that tracks water-level changes in the Hong Kong harbor by employing high-accuracy tide gauges and barometers, among other instruments. The Hong Kong Civil Engineering and Development Department has been responsible for monitoring the settlement of the tide gauge station since 1954. Through conducting levelling measurements from benchmark points established on bedrock to the tide gauge station at varying time intervals ranging from several years to multiple times per year, the HKO adjusts the tide gauge data to account for the effects of settlement [63]. For this study, we used the data from three tide gauges located in the southeast, southwest, and northwest: QUB, SPW, and TBT. The locations of the stations are illustrated in Figure 1, which was created using Digital Elevation Model (DEM) data obtained from the Shuttle Radar Topography Mission (SRTM) by NASA. QUB is situated in the southeastern part of Hong Kong, along the Quarry Bay coast, and is one of the earliest tide gauges established by the HKO, featuring relatively flat terrain. TBT is located in the northwestern part of Hong Kong's New Territories and is the closest station to the Pearl River estuary (PRE) among the six tide gauge stations. It is situated near the estuary of the Kam Tin River, which originates from the central part of Hong Kong, in the Shenzhen Bay area, facing the Shenzhen Futian District to the north. SPW is positioned in the southwestern part of Hong Kong's Lantau Island, in close proximity to the SCS. These data reflect the tidal level above the Chart Datum in centimeters (local sea level), which is 0.146 m lower than the main datum in Hong Kong.

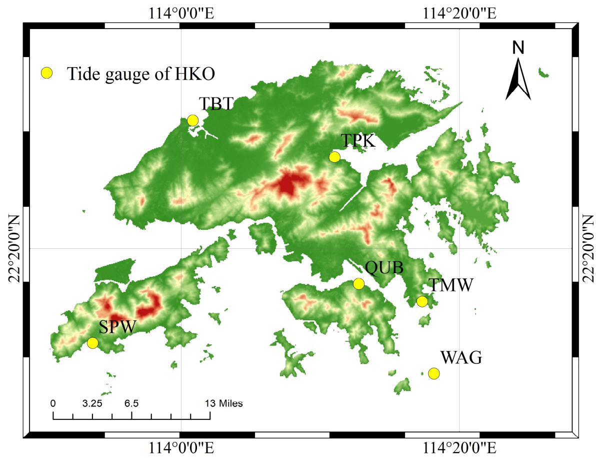

Figure 1. Location of HKO tide gauges (the map was adapted using DEM data from the SRTM by NASA).

The Archiving Validation and Interpretation of Satellite Oceanographic Data (AVISO) dataset is an ocean satellite remote sensing data service jointly developed by the French National Centre for Space Studies (CNES) and the European Space Agency (ESA), aimed at providing global ocean dynamic parameters. It integrates and corrects data from various satellite radar altimeters, such as TOPEX/Poseidon, the Jason series, the ERS series, and Sentinel-3, providing crucial information for researching global ocean circulation, sea-level changes, and climate change. The data type used in this study is Sea Level Anomaly (SLA), which represents the height difference of the sea level relative to the mean sea level. SLA data are obtained by calculating the distance between the sea surface height measured by satellite radar altimeters and the Earth's ellipsoidal surface, correcting it with respect to the geoid, and comparing it to the long-term average sea-level height. SLA data exhibit high spatiotemporal resolution, capable of capturing sea-level changes on short time scales and small spatial scales. We obtained data products from 1 January 2000 to 31 December 2020 with a temporal resolution of 1 day, a spatial resolution of $0.25° \times 0.25°$, and a spatial coverage of 110°~118° E, 20°~24° N. In addition, Southern Oscillation Index (SOI) data were obtained from the National Oceanic and Atmospheric Administration—Climate Prediction Center (NOAA-CPC). The sea-level pressure reanalysis data are from National Centers for Environmental Prediction (NCEP).

2.3. Data Preprocessing

From 2000 to 2020, each tide gauge station counted more than 180,000 data records. Based on our research objectives and expected results, we removed the tidal signal interference in the original data, and then conducted inverse atmospheric correction according to inverted barometer (IB) equation: $IB = -\left(P_{slm} - P_{ref}\right)/\rho g$, where ρ is the seawater density, g is gravity at sea surface, and P_{slm} and P_{ref} are the local and global mean surface pressure values, respectively [64]. Here, we take the mean value of global mid and high latitude sea-level pressure 1013.3 hPa as P_{ref}.

At the same time, according to the research needs, we treated SLA time series as data types averaged day by day, month by month, and year by year.

The specific information of the selected tide gauge stations is presented in Table 1. Our preliminary calculations of the linear sea-level change rates at each station were conducted, with QUB at 2.27 ± 0.26 mm/year, TBT at 3.28 ± 0.26 mm/year, and SPW exhibiting the lowest linear sea-level change rate of 0.54 ± 0.26 mm/year. In terms of data completeness, QUB has the best data integrity, with a missing measurement rate of only 0.36%, while the missing measurement rates for TBT and SPW stations are 4.88% and 5.80%, respectively. The location of most tide gauges is affected by land subsidence, human activities, and other factors, which record the relative changes in sea level. The satellite altimeter measures the absolute change of sea level. The difference between the two is caused by the vertical movement of land. So, we validated the contribution of Hong Kong tide gauge data to the overall sea-level changes in the northern SCS by correlating the data from the three tide gauges with satellite altimeter data. The QUB station exhibited the highest correlation with the AVISO grid data, with an R^2 value of 0.709, while the values for TBT and SPW were 0.648 and 0.629, respectively. Hence, the latter part of this paper will focus on the analysis with the QUB as a representative.

Table 1. Information and linear sea-level change rate of each tide gauge.

Tide Gauge	Location (°)	Missing Rate/%	Linear Rate (mm/year)	R^2
QUB	114.213 E, 22.291 N	0.36	2.27 ± 0.26	0.709
TBT	114.014 E, 22.487 N	4.88	3.28 ± 0.26	0.648
SPW	113.894 E, 22.220 N	5.80	0.54 ± 0.26	0.629

Subsequently, we proceeded with further preprocessing of data from the QUB station, preparing it for utilization in our sea-level prediction model. The dataset was partitioned into a training set and a testing set, where the initial 70% of the data was allocated to the training set and the remaining 30% was designated to the testing set. This distribution ratio was chosen based on experiential knowledge and practice to ensure the model had sufficient data for training while also reserving a portion of data to validate the model's predictive capability. Following this, the data were normalized for input into the model.

2.4. Methods

2.4.1. Ensemble Empirical Mode Decomposition (EEMD)

The EEMD method represents an improvement to the empirical mode decomposition (EMD) [38]. The EMD method can be expressed as follows:

First, all the maxima and minima in the original sequence $x(t)$ are found, and the upper and lower envelopes of the data sequence are obtained by cubic spline interpolation function fitting; the mean value of the upper and lower envelope lines is calculated and recorded as $\overline{x}$, and then subtract $\overline{x}$ from $x(t)$ to obtain a new sequence $x_n(t)$, such as

$$x(t) - \overline{x} = x_n(t) \tag{1}$$

If the obtained $x_n(t)$ still has a negative local maximum and a positive local minimum, it indicates that it is still not an intrinsic mode function (IMF), and further calculation is still required. The formula for this process is as follows:

$$x(t) = \sum_{i=1}^{n} C_i + r_n \tag{2}$$

where $x(t)$ represents the original sequence; C_i denotes the variation sequence with different amplitudes and frequencies, i.e., intrinsic mode functions (IMFs); meanwhile, r_n is the residual term of the original signal after removing all C_i signals [39].

Because EMD has the defect of scale mixing in signal analysis, which leads to the confusion of time and frequency, the decomposition provided by this method is not unique in physics and may even be meaningless. To remedy this problem, the EEMD method based on EMD had appeared. EEMD has not only inherited the advantages of EMD but also avoids the defects that arise from scale mixing. By introducing white noise as auxiliary processing, different time scales can be separated to avoid mode aliasing. Among them, when the original sequence is dominated by high-frequency oscillation, a small-amplitude white noise signal should be added. Conversely, when low-frequency oscillation is dominant in the original sequence, a large-amplitude white noise signal should be added. The calculation steps of this method are as follows:

A group of random white noise sequences $\xi(t)$ is added to the initial sequence $y(t)$ and becomes $Y(t)$

$$Y(t) = y(t) + \xi(t) \tag{3}$$

Perform EMD on $Y(t)$, that is, find all local extreme points of sequence $Y(t)$, and the upper and lower envelope values $Y_{max}(t)$ and $Y_{min}(t)$ of $Y(t)$ are obtained by third-order spline interpolation. Next, average the upper and lower envelope values at each time.

$$m(t) = \frac{Y_{max}(t) + Y_{min}(t)}{2} \tag{4}$$

Then calculate $h(t) = Y(t) - m(t)$, take $h(t)$ as a new signal sequence, and repeat the above calculation until the average envelope close to zero, that is, the intrinsic mode function (IMF). Otherwise, repeat the above process until the conditions are met. Similarly, repeat the above steps for the residual sequence after subtracting IMF_1 from $Y(t)$, so that the eigen modal functions IMF_2, IMF_3, … …, IMF_n are obtained successively, until the residual sequence is monotone function or convex concave function such as

$$Y(t) = \sum_{i=1}^{n} IMF_I(t) + R(t) \tag{5}$$

$IMF_I(t)$ are the IMF components; $R(t)$ is a trend item, representing the change trend of the whole sequence signal.

2.4.2. Multifractal Detrended Fluctuation Analysis (MF-DFA)

In recent years, the multifractal method has been extensively applied in the analysis and prediction of atmospheric and oceanic time series, particularly possessing unique advantages in quantifying the long-range dependence of nonstationary time series such as sea-level changes [65–68]. MF-DFA is an effective method for judging the multifractality of time series based on the elimination of trend fluctuation analysis (DFA) [46,69]. The following discussion describes our application of its basic principle.

For the time series of length N $\{x_k, k = 1, 2, \ldots, N\}$, the sum series of de-averaged values was constructed in the following way:

$$Y(i) = \sum_{k=1}^{i} (x_k - \overline{x}), i = 1, 2, \ldots, N \tag{6}$$

where $\overline{x} = \frac{1}{N} \sum\limits_{k=1}^{N} x_k$.

The new sequence $Y(i)$ was divided into N_s disjoint intervals with a length of s (changing the time scale), where $N_s = int(N/s)$. To ensure that the information at the end of sequence $Y(i)$ would not be lost in the division process, the division process is repeated from the end to solve the problem of missing data at the end, so a total $2N_s$ intervals were obtained.

For s points in each interval $v(v = 1, 2, \ldots, 2N_s)$, the k-order polynomial fitting was carried out by the least square method, and the following was obtained:

$$y_v(i) = a_1 i^k + a_2 i^{k-1} + \ldots + a_k i + a_{k+1} i = 1, 2, \ldots, s; k = 1, 2, \ldots \tag{7}$$

The mean square error $F^2(s, v)$ can be calculated, when $v = 1, 2, \ldots, N_s$

$$F^2(s, v) = \frac{1}{s} \sum_{i=1}^{s} \{Y[(v-1)s + i] - y_v(i)\}^2 \tag{8}$$

When $v = N_s + 1, N_s + 2, \ldots, 2N_s$,

$$F^2(s, v) = \frac{1}{s} \sum_{i=1}^{s} \{Y[N - (v - N_s)s + i] - y_v(i)\}^2 \tag{9}$$

It should be noted that in the fitting process, if the k order polynomial is used, the trend of the $k{-}1^{-1}$ order polynomial in the original sequence can be eliminated, which can ensure that it is not affected by the trend or other nonstationarity and also ensure the reliability of using the fluctuation analysis method.

Then a q-order wave function $F_q(s)$ can be further obtained by the calculation of the wave function $F_q(s)$ of order q that is divided into two cases:

When $q = 0$,

$$F_q(s) = exp\left\{\frac{1}{2N_s} \sum_{v=1}^{N_S} lnF^2(v, s)\right\}, q = 0 \tag{10}$$

When $q \neq 0$,

$$F_q(s) = \left\{\frac{1}{N_s} \sum_{v=1}^{N_S} \left[F^2(v, s)\right]^{\frac{q}{2}}\right\}^{\frac{1}{q}}, q \neq 0 \tag{11}$$

It can be seen from the above formula that $F_q(s)$ is a function of s with respect to v, and through analysis, as s increases, its corresponding $F_q(s)$ will increase in a power–law manner, that is:

$$F_q(s) \sim s^{h(q)} \tag{12}$$

For a long sequence s, the above formula requires $s < \frac{N}{4}$. Because if the length of s is too large, it will inevitably lead to the reduction in the interval number N_s of segments, so that the polynomial fitting by a small number of segment intervals will produce a large statistical error, and eventually lead to an inaccurate estimation of $F_q(s)$.

When $q = 2$, $F_q(s)$ is the standard DFA; after taking logarithms at both ends of the above formula, the corresponding slope is the Hurst exponent $h(q)$ of order q. When the original sequence is a single fractal, the mean square error $F^2(s, v)$ is consistent in all interval scales with length s. Therefore, $h(q)$ is a constant independent of q; when $h(q)$ changes with q, $\{x_k\}$ shows multifractal characteristics. When $h(2) = 0.5$, the original time series $\{x_k\}$ is an independent process or short-range correlation; When $0.5 < h(2) \leq 1$, the sequence has long-range correlation; when $h(2) < 0.5$, the sequence has negative long-range correlation.

Next, the mass exponents $t(q)$ are defined as $t(q) = qh(q) - 1$. From $t(q)$, the multifractal spectrum $D(q)$ is derived using the Legendre transformation, $D(q) = qt(q) - t'(q)$, where $t'(q)$ represents the derivative of $t(q)$ with respect to q. This spectrum $D(q)$ captures the comprehensive scaling behavior within the time series. The width of the spectrum represents the multifractal characteristics of the data. When it is a unimodal function, it indicates that the fractal structure type of the data is relatively simple. Furthermore, the wider the multifractal spectrum, the rougher the signal.

In our study, we set the minimum sub-segment length range to 10 and the maximum to a quarter of the data length. To accurately estimate the multifractal characteristics of the sea-level height time series, we initially analyzed the relationship between the order m and q for the local trend function when fitting different order polynomials. The results indicate that the slopes of the three $lgFq(s) - lgs$ curves are nearly the same when the fitting order m is 1, 2, and 3 at different time scales. Consequently, in this study, the polynomial order for local trend fitting is set to $m = 1$. We then determine the q value range from -10 to 10. Finally, we obtain $H(q)$, $t(q)$, $Dq(q)$, representing the q-th order Hurst index, q-th order detrended fluctuation function, q-th order generalized Hurst index, q-th order singularity spectrum, and q-th order fluctuation function, respectively.

2.4.3. Long Short-Term Memory (LSTM) Neural Network

In this study, we employ a Long Short-Term Memory (LSTM) neural network to model the temporal dynamics of the dataset. LSTM, a particular type of Recurrent Neural Network (RNN), is designed to address the vanishing gradient problem prevalent in traditional RNNs [70]. Hence, in recent years, LSTM has been extensively applied to time series forecasting problems [59,60,71]. The LSTM cell comprises three primary components: an input gate, a forget gate, and an output gate. These gates work in tandem to regulate the flow of information through the cell. Mathematically, the LSTM can be represented as follows.

Firstly, the forget gate is computed, which serves to control which pieces of information from the previous memory cells should be retained and which should be forgotten. The calculation of this gate is accomplished by multiplying the hidden state from the previous time step and the input feature vector at the current time step with certain weights and biases, and subsequently passing the result through a *sigmoid* function. The corresponding formula is as follows:

$$f_t = \sigma\left(W_f[h_{t-1}, x_t] + b_f\right) \tag{13}$$

In this equation, W_f represents the weight matrix, b_f denotes the bias vector, h_{t-1} refers to the hidden state vector at the previous time step, x_t signifies the input feature vector at the current time step, and σ corresponds to the *sigmoid* function. The role of the forget gate is to regulate which pieces of information from the previous memory cells can be transmitted to the memory cells at the current time step.

The output gate assists in determining which pieces of information should be added to the memory cells. This gate consists of two components: a *sigmoid* function and a *tanh* function. The *sigmoid* function determines which information is required to be added, while the *tanh* function is employed to calculate the values of the information to be incorporated. The respective formula is:

$$i_t = \sigma(W_i[h_{t-1}, x_t] + b_i) \tag{14}$$

$$\widetilde{C}_t = \tanh(W_C[h_{t-1}, x_t] + b_C) \tag{15}$$

In this equation, W_i, b_i, W_C, and b_C represent the weight matrices and bias vectors, while tanh denotes the hyperbolic tangent function. The role of the input gate is to control which pieces of information at the current time step can be added to the memory cells.

Subsequently, the memory cell state must be updated. This is achieved through a weighted sum of the information controlled by the forget gate and the input gate, with the new state replacing the previous memory cell state:

$$C_t = f_t C_{t-1} + i_t \widetilde{C}_t \tag{16}$$

The state of the memory cells is formed by a combination of the previous memory cell state and the information controlled by the input and forget gates at the current time step.

Lastly, the output gate computation is performed to determine which pieces of information should be output from the memory cells. The calculation of this gate is similar to that of the forget gate and the input gate; however, it employs the tanh function to compute the values of the information to be output. The result of the output gate is multiplied by the output of the *tanh* function, generating the hidden state:

$$o_t = \sigma(W_o[h_{t-1}, x_t] + b_o) \tag{17}$$

$$h_t = o_t * \tanh(C_t) \tag{18}$$

The role of the output gate is to determine which pieces of information should be output from the memory cells at the current time step, with the hidden state being a combination of the information controlled by the output gate and the memory cell state at the current time step.

During the testing process, the LSTM neural network can be utilized for sequence data prediction. Given a historical sequence of data, the LSTM neural network takes it as input and computes the output gate and memory cell state through forward propagation. Subsequently, the prediction results are derived based on the information controlled by the output gate. Thus, the predictive capability of the LSTM neural network is manifested in its ability to output a prediction at each time step t, and to use historical sequence data to forecast future values. This capacity for long-term memory and selective processing renders the LSTM particularly powerful in handling time series data.

Upon completion of the training and validation processes, the performance of the LSTM model is evaluated using established metrics, such as the root mean squared error (RMSE), coefficient of determination (R^2), and the mean absolute error (MAE). The model's ability to accurately capture the temporal dynamics of the dataset is then analyzed and compared to alternative approaches, providing valuable insights into the efficacy of the LSTM architecture for this particular problem domain.

3. Results and Discussion

3.1. EEMD Analysis Results

We initially conducted an EEMD analysis on the daily resolution time series data from tidal stations situated in the southeast (QUB), northwest (TBT), and southwest (SPW) regions of Hong Kong waters, obtaining 11 IMF components and a residual (RES), as illustrated in Figures 2–4. All components successfully passed the 99% significance test. Furthermore, we calculated the period, variance contribution rate, and correlation coefficient between each component and the original series, which are presented in Table 2.

Table 2. The corresponding period, variance contribution rate, and correlation coefficient of the modes obtained from EEMD analysis by QUB, TBT, and SPW.

IMFs	QUB			TBT			SPW		
	Period (Year)	Variance Contribution (%)	Correlation Coefficient	Period (Year)	Variance Contribution (%)	Correlation Coefficient	Period (Year)	Variance Contribution (%)	Correlation Coefficient
IMF1	0.01	11.47	0.42	0.01	12.48	0.43	0.01	11.86	0.42
IMF2	0.02	10.95	0.53	0.02	9.29	0.48	0.02	11.24	0.53
IMF3	0.04	10.26	0.50	0.04	8.23	0.45	0.04	9.97	0.50
IMF4	0.09	5.82	0.42	0.08	4.48	0.37	0.08	5.67	0.42
IMF5	0.17	6.63	0.39	0.16	5.04	0.34	0.18	6.76	0.39
IMF6	0.34	3.62	0.42	0.35	5.66	0.45	0.36	4.75	0.43
IMF7	0.91	12.54	0.44	0.96	15.15	0.48	0.91	13.55	0.45
IMF8	1.75	1.77	0.21	1.91	5.56	0.22	1.91	2.07	0.18
IMF9	3.00	1.31	0.14	4.20	2.32	0.09	4.20	2.31	0.16
IMF10	7.01	0.61	0.11	10.51	2.40	0.11	10.51	0.36	0.08
IMF11	21.02	1.26	0.15	21.02	2.72	0.09	21.02	0.28	0.01

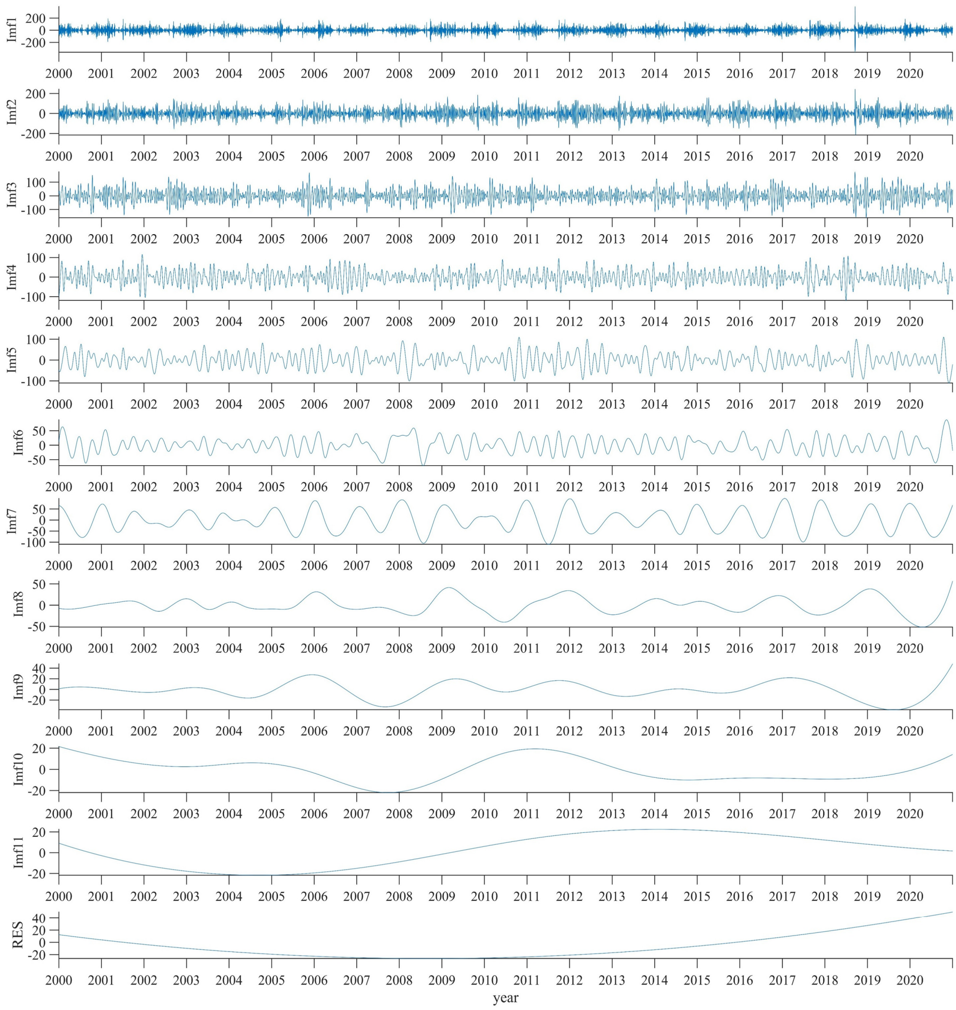

Figure 2. EEMD results of QUB: displaying the 11 IMFs from high to low frequency with the residual at the bottom.

Taking QUB as an example, the first four high-frequency signals obtained after EEMD represent high-frequency variations in sea level, all of which possess relatively short periods. The oscillatory characteristics of these high-frequency signals in the time series may reflect the interactive effects of various complex physical processes in the ocean. However, since high-frequency signals have relatively short periods and smaller amplitudes, their physical significance may not be as evident as that of low-frequency signals, making them difficult to interpret individually. The oscillation periods of IMF5 and IMF6 lie between 2 and 5 months, which are commonly considered as seasonal fluctuations under the influence of monsoons in the SCS region. Seasonal fluctuations in this area are primarily induced by summer and winter monsoons, which generate oceanic internal waves with specific frequencies through seawater movement and mixing processes. These internal waves propagate through shallow areas in the SCS, forming signals with periods of 2–5 months in the sea-level height time series. The IMF7 component, which accounts for the highest variance contribution, corresponds to a period of 0.91 years, indicating its most significant contribution to sea-level change behavior. Based on previous research and atmospheric-ocean dynamics theory, it can be inferred that the primary factor causing this period is seasonal [72]. Seasonal variations are primarily influenced by factors such as atmospheric pressure, wind stress, seawater temperature, and salinity. The interaction and variation of these factors lead to seasonal fluctuations in the sea level of the SCS. In the northern SCS, the sea level is relatively higher in winter and lower in summer. This is mainly due to the influence of winter monsoons, which transport seawater from the southern to the northern

SCS, resulting in a rise in sea level [73]. In recent years, the intensity of monsoon activity along the northern SCS coast demonstrates a more pronounced weakening trend during the summer and autumn [74]. Additionally, in the nearshore areas of the northern SCS, the annual average wind speed is on a downward trend [75]. The oscillation periods of IMF8 (1.75 years), IMF9 (3.00 years), and IMF10 (7.01 years) are commonly considered to be associated with El Niño/La Niña events, which are influenced by temperature changes in the Pacific Ocean. When El Niño occurs, the sea-level height in the northern South China Sea typically rises, while it generally decreases during La Niña events. The emergence of this phenomenon is often attributed to factors such as water mass transport and wind field changes induced by ENSO. Periods of around 10 years for IMF10 (10.51 years) and around 20 years for IMF11 (20.02 years) are often linked to the Pacific Decadal Oscillation (PDO) and Interdecadal Pacific Oscillation (IPO), respectively. The magnitude and increasing or decreasing trend of the RES component can reflect the overall changes in sea level. Overall, based on the results of the RES, it can be observed that the sea-level changes in the area measured by QUB generally exhibit a rising trend, which is consistent with the long-term rising trend of global sea levels over the past few decades.

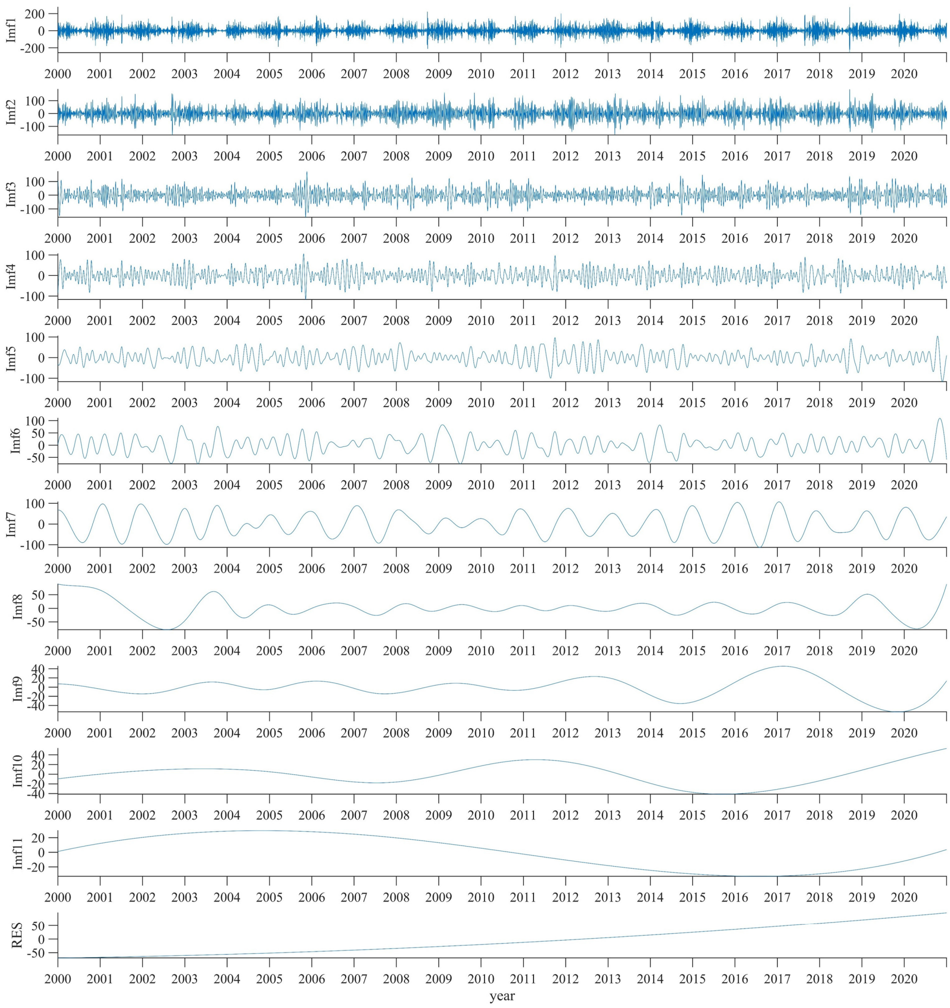

Figure 3. EEMD results of TBT: displaying the 11 IMFs from high to low frequency with the residual at the bottom.

Figures 3 and 4 present the EEMD analysis results for TBT and SPW, respectively. In conjunction with Table 2, the components derived exhibit similar characteristics to those of QUB. The trend components indicate that both stations exhibit rising sea levels, with TBT's rising trend being more pronounced than that of SPW. The calculated sea-level change rate for TBT is about 7.84 mm/year. This phenomenon may be associated with its geographic location near the upstream region of the PRE, which results in a significant influence from fluvial inputs. Additionally, the station is situated in Shenzhen Bay, where large-scale land reclamation activities over the past few decades have contributed to the acceleration of sea-level rise to some extent [14]. Furthermore, by comparing the periods obtained from the EEMD decomposition of the three tidal stations, it can be observed that the sea-level change period at QUB is shorter than those of the other two stations. This is due to QUB being located within a bay on the north shore of Hong Kong Island and surrounded by the island and mountain ranges of the north shore, thus reducing the influence of external ocean currents and tidal waves. Additionally, according to the data from the Hong Kong Lands Department, the water depth of QUB is approximately 5–10 m, relatively shallow, resulting in smaller tidal wave amplitudes and periods.

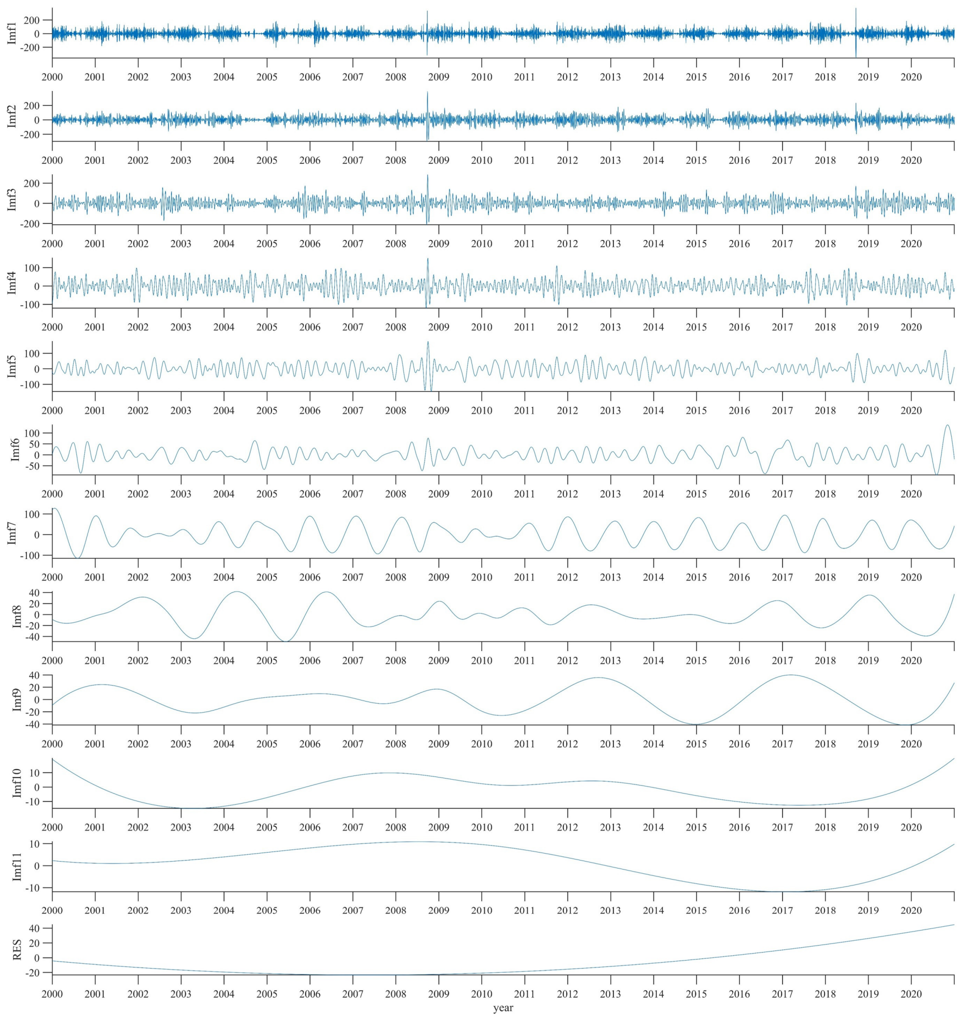

Figure 4. EEMD results of SPW: displaying the 11 IMFs from high to low frequency with the residual at the bottom.

Regarding the spatial distribution and variation of sea-level change rates, we conducted EEMD on the time series for each grid point within the study area, extracted the trend components from the decomposition results, and calculated the discrete derivatives over time. Subsequently, we averaged these values to obtain the mean sea-level change rate for each grid point, ultimately yielding a spatial distribution map of the mean sea-level anomaly change rate for the northern SCS based on EEMD (Figure 5). The trend components derived from the EEMD demonstrate a relatively higher sea-level rise rate along the Guangdong coast compared to offshore areas, with an especially elevated rise rate in the eastern PRE. In addition, the rise rate in the western Pearl River Estuary and the coast area near to Leizhou peninsula is relatively low. Focusing on the sea level in Hong Kong, its rising rate shows a slightly faster distribution in the east than in the west. Spatially, the northern SCS exhibits an overall rising trend in sea level, yet this trend is unevenly distributed. This uneven spatial distribution may be related to the activity of ocean currents and eddies. In regions with active ocean currents and eddies, there is a larger magnitude of local sea-level rise. This could be attributed to the ability of ocean currents and eddies to transport and redistribute a significant amount of heat and salinity in the ocean, thereby influencing the thermal content and density distribution of the ocean and further impacting sea-level variations [76].

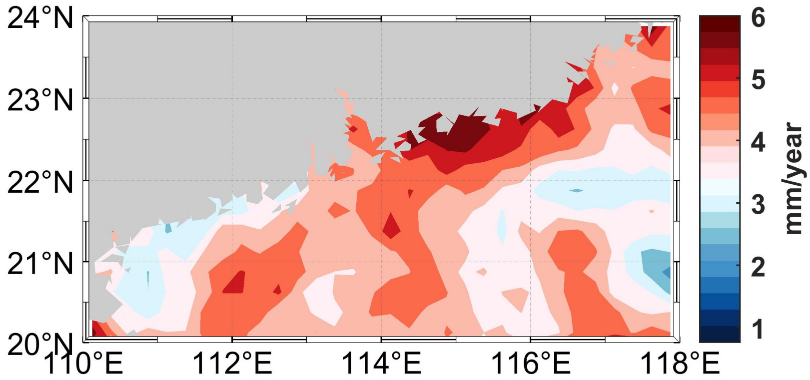

Figure 5. Spatial distribution of sea-level change rate in the northern SCS, based on satellite altimetry data.

3.2. Analysis of the Impact of ENSO on Sea-Level Change

Sea-level changes are influenced by a multitude of factors, such as land subsidence, reclamation, and global climate change. Among these, the impact of global climate change on sea level is both long term and periodic, which is also manifested in the study area. Furthermore, the study area is located in the western Pacific and is therefore significantly affected by ENSO, which exhibits quasi-periodicity with a cycle of 2–7 years [18,34,77,78]. To more explicitly analyze this influence, the IMF8, IMF9, and IMF10 components corresponding to the period of QUB are superimposed and reconstructed, and subsequently denoted as IMF8-10. It is compared with the contemporaneous SOI (Figure 6). The SOI reflects the activity of the El Niño phenomenon. A continuous negative SOI indicates the occurrence of an El Niño event, whereas a positive value signifies a La Niña event. Time-lead lag correlation analysis reveals that the highest correlation between the IMF8-10 signal and the SOI index is 0.36 (with a sea-level delay of 6 months), indicating a response time delay of 6 months between the signal delay and the El Niño, which is higher than the original correlation coefficient of 0.15 between the signal and the SOI (Figure 7). This result demonstrates that ENSO exerts a certain influence on sea-level changes in the study area. The impact of the ENSO phenomenon on sea-level anomalies in the northern coastal waters of the SCS can be succinctly summarized as follows: ENSO initially induces trade wind anomalies. In the case of negative anomalies, southward wind field anomalies are observed, prompting the generation of westward currents due to the wind-driven current mechanism. This, in turn, leads to volume transport between the SCS and adjacent oceans, as well as anomalous Ekman pumping, ultimately resulting in elevated sea levels in areas of seawater convergence. Conversely, positive anomalies produce the opposite effect. In essence, during El Niño periods, the sea-level height in the northern SCS decreases, while it exhibits an upward trend during La Niña periods. Furthermore, mass exchange, predominantly governed by precipitation, plays a more critical role in the persistence of negative sea-level anomalies in subsequent periods [18,33,79].

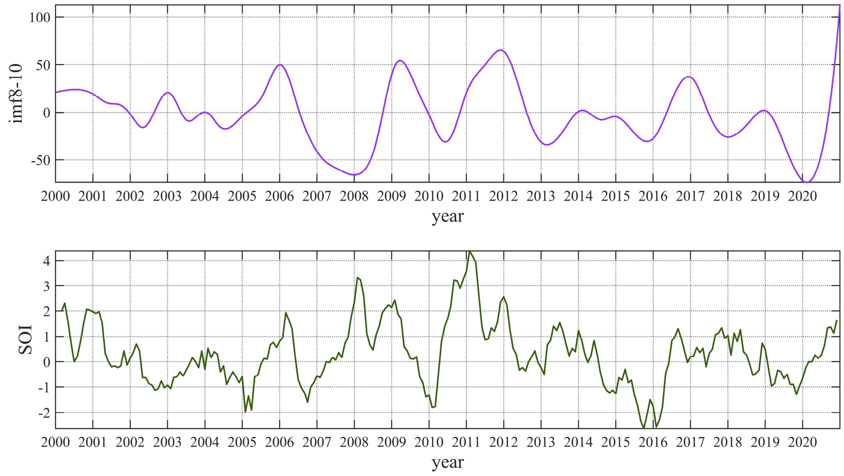

Figure 6. Comparison of IMF 810 and SOI (3month running filter).

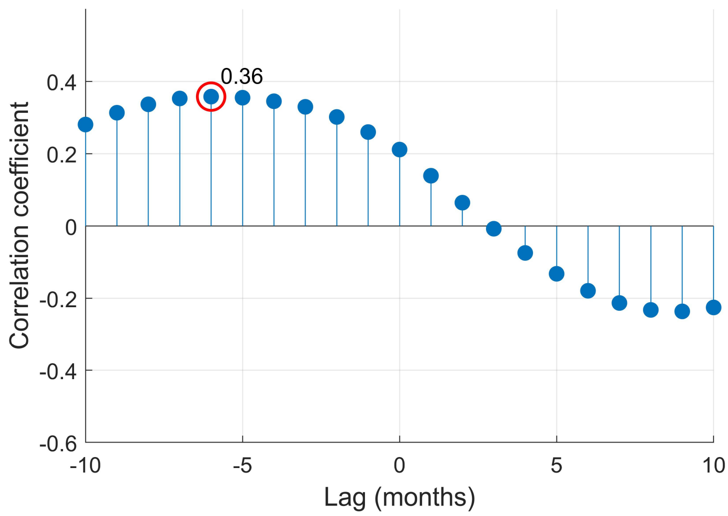

Figure 7. Time lag correlation between IMF810 and SOI.

3.3. MF-DFA Analysis Results

We adopt MF-DFA analysis on the daily sea-level height time series of three tidal stations to determine their multifractal characteristics and long-range correlation, which is also a better foundation for the sea-level prediction.

Figure 8 presents the $lgFq(s) - lgs$ relationships as a function of q for the sea-level time series measured by the QUB, TBT, and SPW tidal stations. The horizontal axis represents the sub-segment length of the time series, and the vertical axis represents the logarithm of the corresponding $Fq(s)$ values, where $Fq(s)$ is the q-th order function of the time series with a sub-segment length of s. When the time series exhibits multifractal characteristics, the curve assumes an approximate linear relationship, with the linear slope representing the Hurst index of the time series. From top to bottom, the curves in the figure correspond to $q = 10,\ q = 8,\ q = 6,\ \ldots,\ q = -10$. It can be observed that for different values of q, the curves corresponding to each tidal station exhibit a distinct linear trend. Through calculation, their corresponding R^2 values are all greater than 0.9, and the fitted lines satisfy statistical tests. This demonstrates that the sea-level time series of the three tidal stations possess multifractal characteristics, i.e., long-range correlations over multiple scales, indicating that the time series exhibit similar statistical patterns at different time scales.

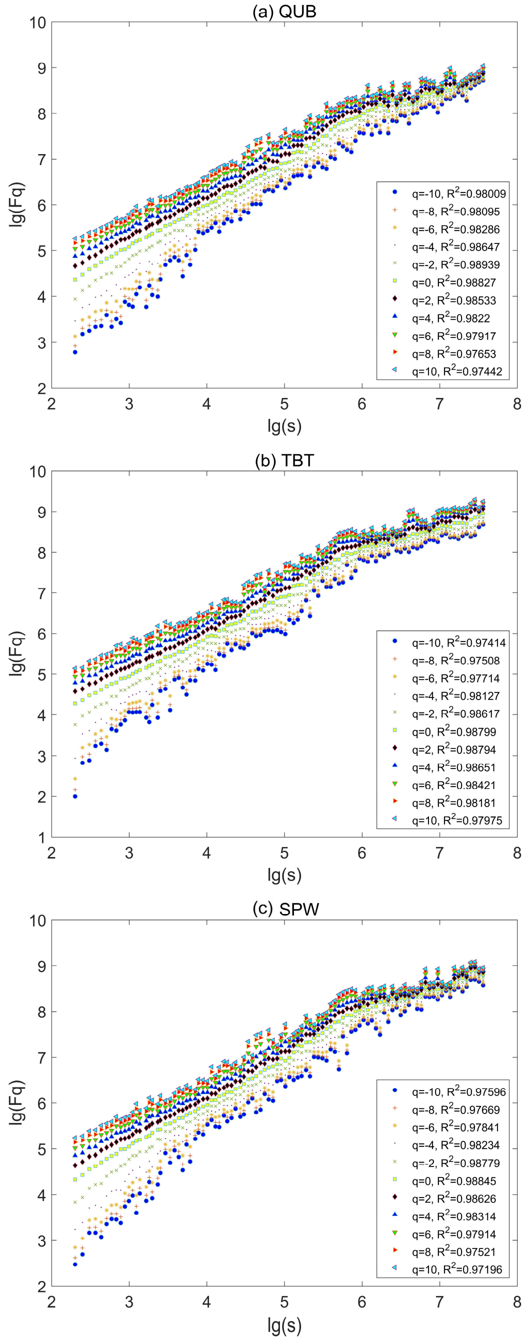

Figure 8. $lgFq(s) - lgs$ diagrams of QUB, TBT, and SPW.

Subsequently, through the MF-DFA analysis, the generalized Hurst exponent plots ($q - H(q)$), mass exponent plots ($q - t(q)$), and multifractal spectra ($hq - D(q)$) corresponding to the three tidal stations were obtained, as illustrated in Figures 9–11, respectively. $H(q)$ is the generalized definition of the q-th order Hurst exponent, which reflects the long-term dependence and self-similarity of data on different time scales. In Figure 9, the horizontal axis represents the q values, and the vertical axis represents the corresponding $H(q)$ values, that is, the q-th order Hurst exponent. From the figure, the relationship between $H(q) - q$ for all three stations is nonlinear, and when $q = 2$, the corresponding $H(q)$ for QUB, TBT, and SPW are 0.83, 0.91, and 0.86, respectively, all greater than 0.5, indicating that all of the time series possess multifractal characteristics and long-range correlations.

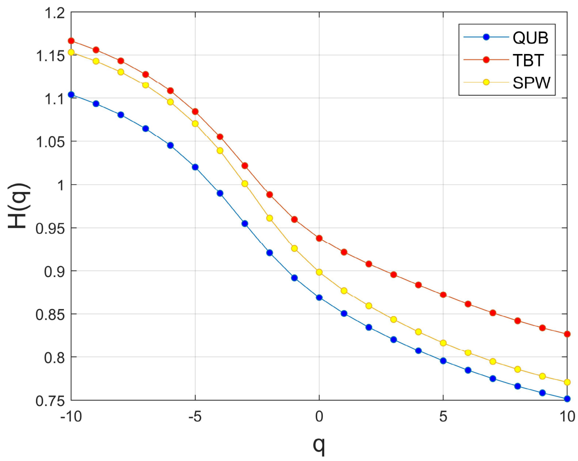

Figure 9. The generalized Hurst exponent plots of QUB, TBT, and SPW.

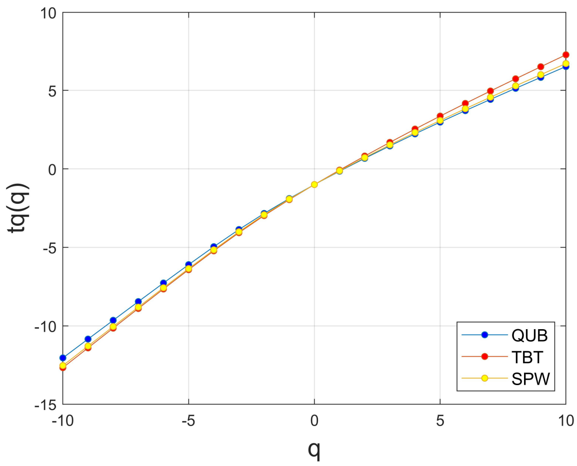

Figure 10. The scaling exponent plots of QUB, TBT, and SPW.

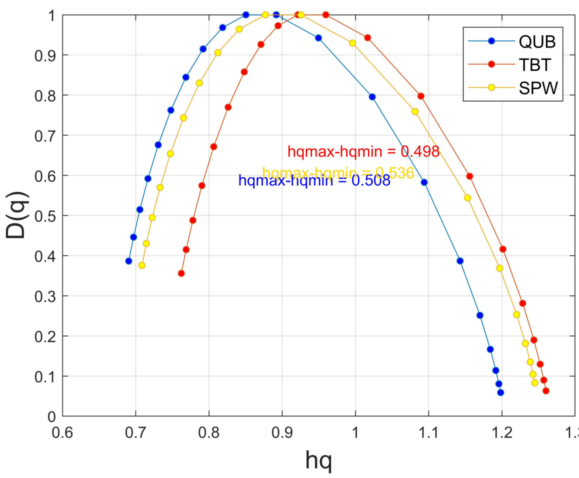

Figure 11. The multifractal spectrum plots of QUB, TBT, and SPW.

The scaling exponent $t(q)$ is used to determine the fractal characteristics of a signal. In the $q - t(q)$ plot, the q values are plotted on the horizontal axis, and the $t(q)$ values, i.e., the q-th order detrended fluctuation functions, are plotted on the vertical axis, forming a curve. The shape of this curve reflects the fractal features of the data. If $t(q)$ is a straight line, then the signal function is monofractal; if $t(q)$ is nonlinear, then the signal function is multifractal. As seen in Figure 10, there are evident nonlinear relationships between q and $t(q)$ for the three tidal stations, further indicating that the sea-level height time series possess strong multifractal properties.

The $hq - D(q)$ relationship plot, also known as the multifractal spectrum of the signal, is one of the main outcomes of fractal analysis. Through the analysis of the multifractal spectra (Figure 11) of the daily time series of the three tidal stations, it was found that they are all unimodal functions. The spectral widths $hq_{max} - hq_{min}$ for QUB, TBT, and SPW are 0.508, 0.498, and 0.536, respectively, further demonstrating that the sea-level fluctuations at each tidal station exhibit multifractal characteristics.

From the analysis, it is evident that the sea-level changes measured at the QUB, TBT, and SPW tide gauges exhibit certain multifractal characteristics and long-range correlations. Among these three stations, the multifractal features are relatively strong at SPW in the southwest, while the features at TBT in the northwest are weaker compared to the other stations. The reason for this phenomenon might be that SPW is closer to the SCS, and thus is more significantly influenced by oceanic dynamic processes such as the SCS circulation and seasonal effects. In addition, the population of TBT in Hong Kong is relatively sparse, with a lower level of development, which results in sea-level changes being less influenced by human activities. On the other hand, TBT is located in Shenzhen Bay, at the mouth of the Kam Tin River in Hong Kong and near the PRE, making it less susceptible to the atmospheric and oceanic changes in the SCS.

3.4. Prediction of Sea Level in the Northern South China Sea Based on EEMD-LSTM

To predict the sea level based on tide gauge data, an LSTM model architecture was constructed, including a sequential input layer, an LSTM layer, a Rectified Linear Unit activation (ReLU) layer, a fully connected layer, and a regression layer. Furthermore, we established the model parameters, employing the Adam gradient descent algorithm, with a maximum number of training iterations set at 500 and an initial learning rate of 0.001. We employed a piecewise adjustment strategy for reducing the learning rate, setting the learning rate decay factor to 0.5, and initiating a decrease in the learning rate after 100 training iterations. Following the input of normalized sea-level height data from QUB into the LSTM model, it was trained, and simulation predictions were carried out for both the training and testing sets. The prediction results were then de-normalized, with the outcomes for the training and testing sets depicted in Figure 12. The red curve represents the actual values, while the blue curve signifies the predicted values. The training set's root mean square error (RMSE) was 76.61, the coefficient of determination (R^2) was 0.69, and the mean absolute error (MAE) was 57.34. The testing set exhibited an RMSE of 81.06, and an MAE of 59.22, with units in millimeters. In addition, the R^2 was 0.67.

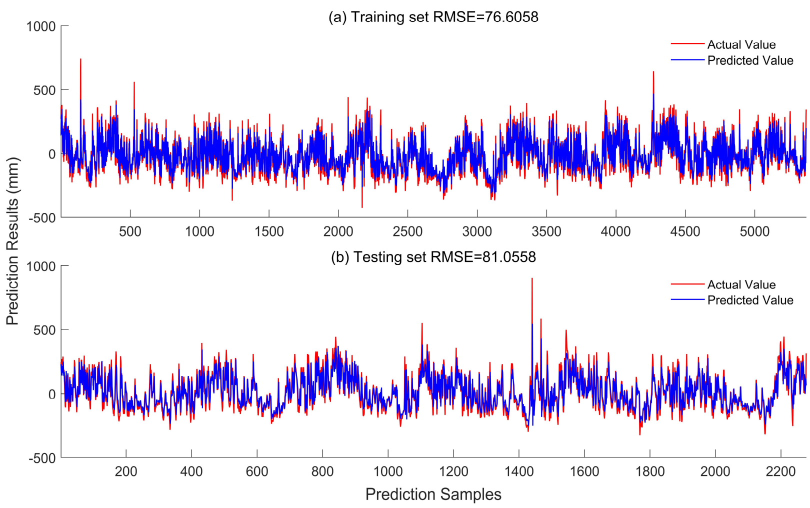

Figure 12. QUB's daily average data LSTM prediction results: (**a**) training set, (**b**) testing set.

The correlation and residuals serve as essential tools for evaluating the performance of the predictive models. Figure 13 displays the correlation scatterplots (a) and residual plots (c) of the actual and predicted values for the training set obtained from the QUB station data after LSTM training, as well as the correlation scatterplots (b) and residual plots (d) for the testing set. According to the correlation scatterplots of both the training and testing sets, there is a certain linear relationship between the predicted and actual values. However, this relationship is not particularly pronounced, as the R^2 of the fitted line is relatively low, indicating that the model's fitting performance for the sample data is less than ideal. In the residual plots, the points represent the prediction errors of the sample points. The distribution of the points is wide and sparse, indicating that the model's prediction errors are relatively large.

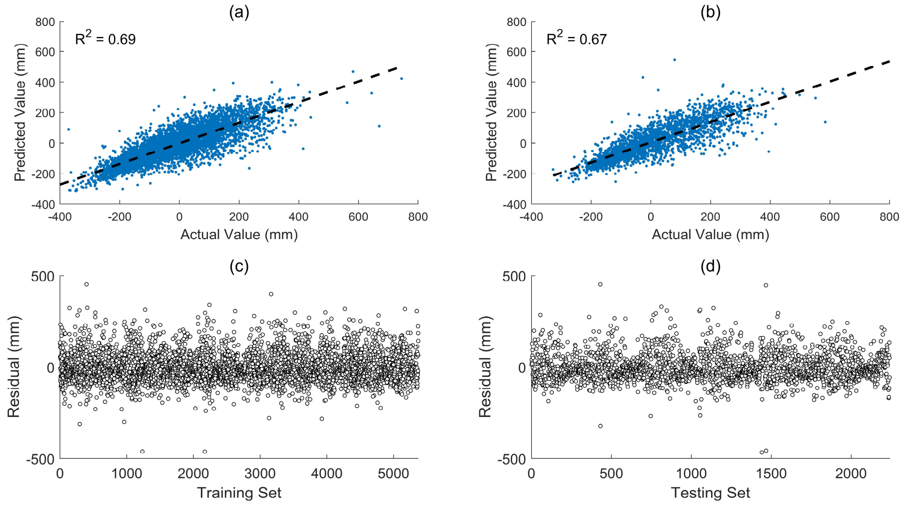

Figure 13. Scatterplots and residual plots of the LSTM training set are presented in (**a**,**c**), respectively. Similarly, (**b**,**d**) show the corresponding scatterplots and residual plots of the testing set predictions.

These results demonstrate that although LSTM can be applied to a certain extent in predicting sea-level changes in tide gauge data, the fitting results for both the training and testing sets are not entirely satisfactory. The model exhibits considerable prediction errors in both sets and fails to fit the data effectively. Consequently, there remains room for further improvement in its predictive performance.

Figure 14 provides the flowchart of the EEMD-LSTM modeling process. Firstly, the sea-level height data from QUB are decomposed through EEMD, resulting in 11 IMFs and residual components (which is the result obtained in Section 3.1). Similarly, the first 70% of these data are partitioned into a training set and the latter 30% into a test set. Afterwards, these data are normalized and individually input into the model for LSTM training. In order to achieve more accurate prediction results, the parameters such as the maximum training iteration, initial learning rate, and learning rate decay factor are appropriately adjusted based on the performance of each component during training. Finally, the results obtained from these components are denormalized and stacked for reconstruction to obtain the final predictions of the EEMD-LSTM model.

The comparison between the predicted values of IMF1-11 and RES and the original data is illustrated in Figure 15, while the evaluation indices for each component are presented in Table 3. As can be observed from the figure and table, the fitting performance of the high-frequency component IMF1 is relatively poor compared to the other components. Nevertheless, its amplitude and trend are consistent with the variations in the original data. However, for IMF2 through IMF11 and RES, the model's predictive performance gradually improves as the component variations tend toward stability.

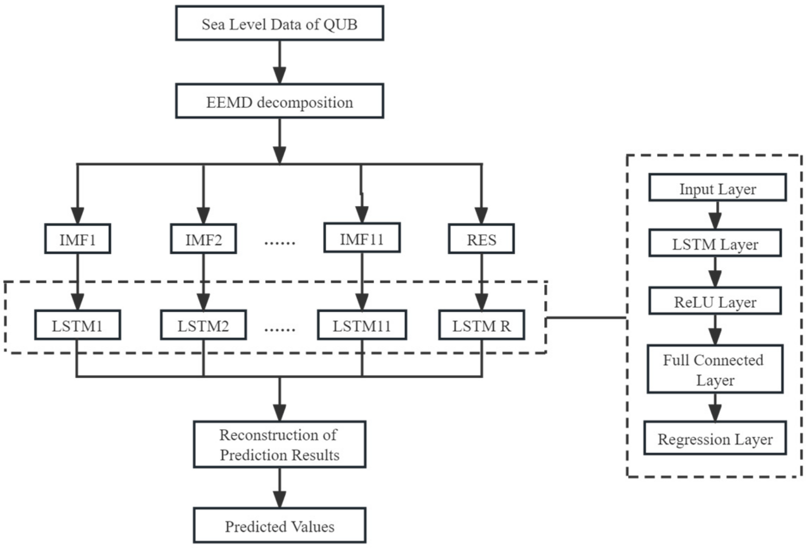

Figure 14. Flowchart of the EEMD-LSTM sea-level prediction model.

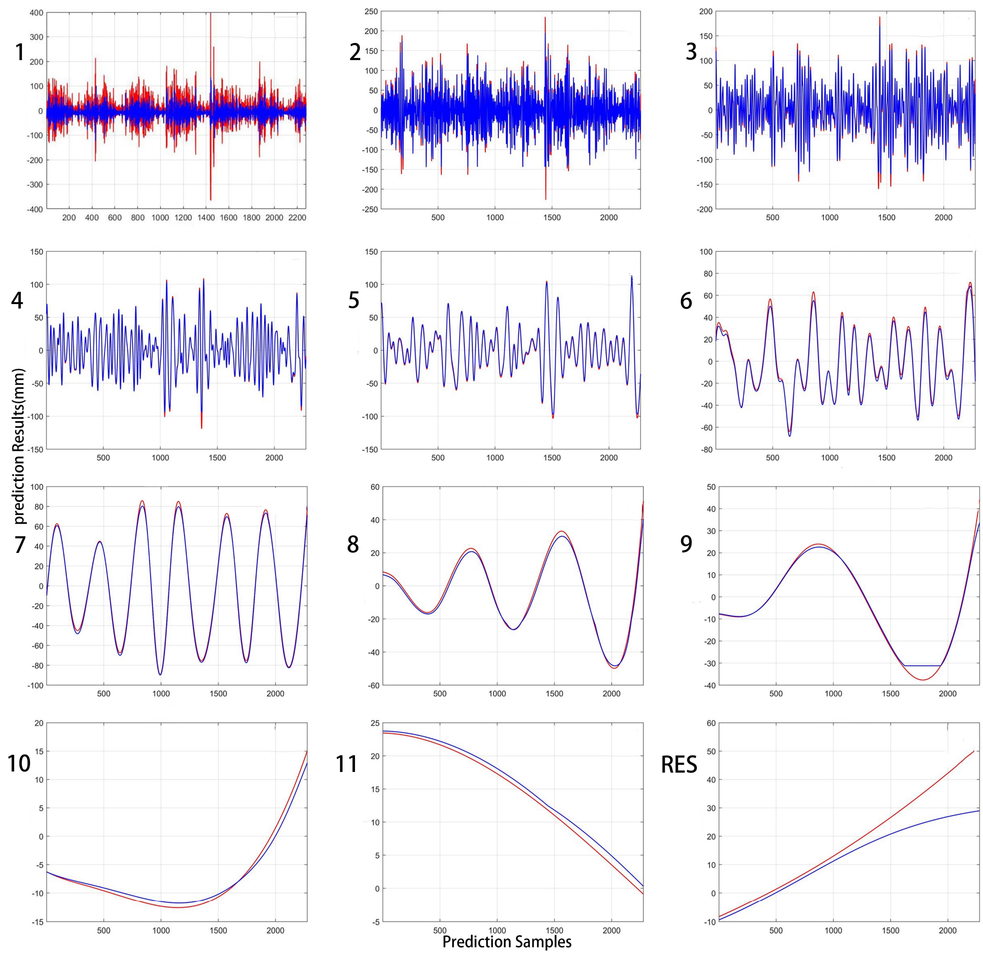

Figure 15. Comparative display of the predicted versus actual values across eleven different IMF components (1–11) and the residual (RES) in the testing sets.

Table 3. Evaluation metrics data for each IMF components testing sets.

	IMF1	IMF2	IMF3	IMF4	IMF5	IMF6	IMF7	IMF8	IMF9	IMF10	IMF11	RES
RMSE	46.37	10.09	4.98	1.89	2.38	3.54	2.65	2.06	2.17	0.84	0.88	8.48
R^2	0.26	0.96	0.99	0.99	0.99	0.99	0.99	0.99	0.99	0.99	0.97	0.76
MAE	30.40	7.28	3.98	1.25	2.13	2.94	2.39	1.68	1.29	0.82	1.28	5.84

The results of the EEMD-LSTM model for both the training and testing sets are depicted in Figure 16, with the actual values and predicted values represented by red and blue curves, respectively. The training set yielded an RMSE of 40.15, an R^2 of 0.91, and an MAE of 28.74, while the testing set exhibited an RMSE of 48.79, an R^2 of 0.88, and an MAE of 34.21, with units in millimeters. By comparing the training and testing sets with the original data, we can discern that the model possesses a robust predictive capability, enabling it to accurately forecast sea-level changes.

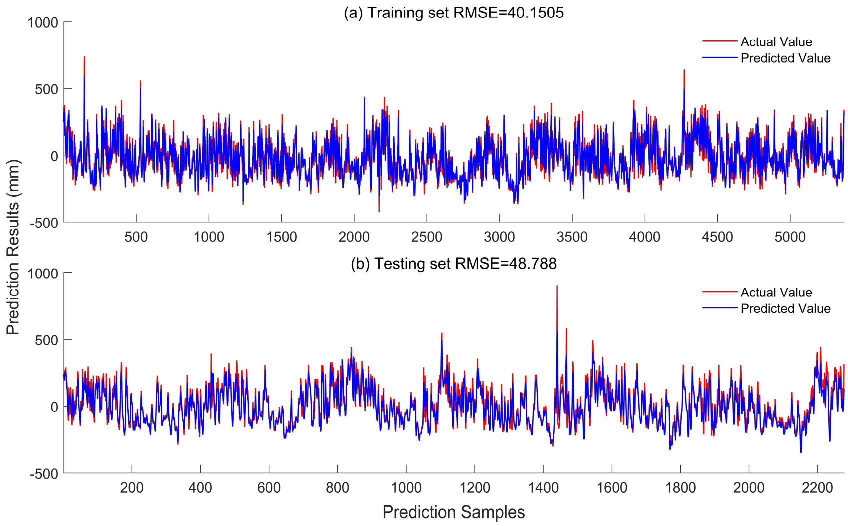

Figure 16. QUB's daily average data EEMDLSTM prediction results: (**a**) training set, (**b**) testing set.

To evaluate the predictive performance of the EEMD-LSTM model, Figure 17 presents the correlation scatterplots (a,b) and residual plots (c,d) for both the training and testing sets. We can observe that the correlation between the predicted and actual values is relatively strong, with the coefficient of determination (R^2) reaching 0.91 for the training set and 0.88 for the testing set. Compared to the LSTM model (Table 4), this model can better capture the regularities in the data and accurately predict their variations. The residual plot also exhibits a relatively concentrated distribution pattern.

Table 4. Comparison of evaluation metrics for the training and testing sets between LSTM and EEMD-LSTM.

	RMSE/mm	R^2	MAE/mm
LSTM-Training	76.61	0.69	57.34
LSTM-Testing	81.06	0.67	59.22
EEMD-LSTM-Training	40.15	0.91	28.74
EEMD-LSTM-Testing	48.79	0.88	34.21

This indicates that the error distribution between the model's predicted results and the actual values is uniform, with no systematic biases or outliers present. Consequently, the overall prediction results of the EEMD-LSTM model are satisfactory.

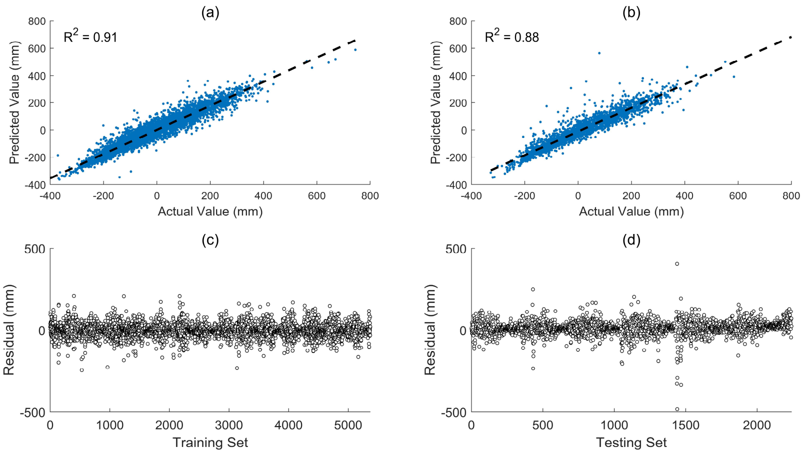

Figure 17. Scatterplots and residual plots of the EEMDLSTM training set are presented in (**a**,**c**), respectively. Similarly, (**b**,**d**) show the corresponding scatterplots and residual plots of the testing set predictions.

4. Conclusions

In this study, we employed EEMD analysis to examine sea-level changes in three regions of Hong Kong waters using daily resolution time series data from tidal stations. The results of QUB identified 11 IMF components and an RES, which revealed the intricate interplay of multiple physical processes within the ocean. High-frequency signals with short periods were observed, but their interpretation remains challenging due to their small amplitudes. Low-frequency signals (IMF5 to IMF11) offered more discernible insights into the driving factors of sea-level changes. Seasonal fluctuations were identified in IMF5 and IMF6, while the IMF7 component potentially reflects the impact of seasonal wind field changes on the sea-level height. The oscillation periods of IMF8, IMF9, and IMF10 were associated with El Niño/La Niña events, and the periods of IMF10 and IMF11 were linked to the Pacific PDO and IPO, respectively. Similar characteristics were observed in the EEMD analysis results for the other two regions, both of which exhibit rising sea levels. A spatial distribution map of the mean sea-level anomaly change rate in the northern South China Sea, derived from the EEMD analysis, revealed a spatially uneven distribution of the sea-level change trend. Specifically, the distribution pattern shows that the eastern PRE is faster than the western, and the eastern Hong Kong is also faster than the western. In addition, this study discusses the relationship between ENSO and sea level in the northern SCS and finds a 6-month lagged correlation between the signals. This finding highlights the importance of considering the effects of ENSO and other climatic factors in the analysis of sea-level changes.

This study also employs MF-DFA analysis on daily sea-level height time series from three tidal stations to determine the multifractal characteristics and long-range correlation. The generalized Hurst exponent, mass exponent, and multifractal spectra plots further confirm the multifractal characteristics of the sea-level height time series. All three stations exhibit nonlinear $H(q) - q$ relationships, indicating the presence of multifractal features and long-range correlations. The results indicate that the sea-level time series of the three stations possess multifractal characteristics and long-range correlations across multiple scales. The multifractal features are relatively strong at SPW in the southwest and weaker at TBT in the northwest. The differences in the multifractal characteristics between the stations may be attributed to their geographical locations and surrounding influences. SPW's proximity to the SCS makes it more susceptible to oceanic dynamic processes such as SCS circulation and seasonal effects. In contrast, TBT is situated near the PRE and is less affected by atmospheric and oceanic changes in the SCS. Additionally, TBT has a lower level of development and a sparser population, resulting in less influence from human activities. Understanding the multifractal characteristics and long-term correlations of sea-level time series can provide the scientific basis for further predicting sea-level changes and enhance our comprehension of the driving factors behind sea-level variations.

At last, we propose an improved sea-level prediction method based on EEMD and LSTM and explore the predictive performance of LSTM and EEMD-LSTM models using daily sea-level data from the QUB. While the LSTM model demonstrated some potential in predicting sea-level changes, the fitting results for both the training and testing sets were not entirely satisfactory, revealing considerable prediction errors and suboptimal data fitting. The EEMD-LSTM model exhibited a significantly better predictive capability, with higher R^2 values for both the training and testing sets, suggesting its ability to accurately forecast sea-level changes. The correlation scatterplots and residual plots further confirmed the robustness of the EEMD-LSTM model, demonstrating a strong correlation between the predicted and actual values and a relatively good distribution of residuals, indicative of a uniform error distribution without systematic biases or outliers. These findings imply that the EEMD-LSTM model is more suitable for predicting sea-level changes in the northern SCS region, as exemplified by Hong Kong. By capturing the regularities in the data more effectively and accurately predicting their variations, the EEMD-LSTM model can contribute to a better understanding of the patterns and trends in sea-level changes in this area.

In summary, this study demonstrated the usefulness of employing EEMD, MF-DFA analysis, and the EEMD-LSTM model to investigate the multiscale characteristics of sea-level changes in the northern South China Sea region and proposed an improved sea-level prediction method. Our findings provide valuable insights into the driving factors behind these changes and support future efforts to assess the flooding risk in low-lying coastal areas along the northern SCS. Further research can focus on refining the EEMD-LSTM model by incorporating other variables such as other climate indices or anthropogenic factors, to improve its predictive accuracy and applicability to a wider range of coastal areas and assess the future flooding risk of coastal cities along the northern SCS.

Author Contributions: Conceptualization, Y.Z. and Y.Y.; methodology, Q.C.; software, J.-Y.T.; validation, Y.Y., Q.C. and Y.Z.; formal analysis, Y.Y. and Q.C.; investigation, Y.Y. and K.-P.W.; resources, J.-Y.T. and K.-P.W.; data curation, Y.Z. and K.-P.W.; writing—original draft preparation, Y.Y.; writing—review and editing, Q.C. and Y.Z.; visualization, Y.Y and Y.M.; supervision, Y.Z. and Q.C.; project administration, Y.Z.; funding acquisition, Y.Z. All authors have read and agreed to the published version of the manuscript.

Funding: This research was funded by the Marine Special Program of Jiangsu Province in China (JSZRHYKJ202007), the National Natural Science Foundation (U1901215), the Natural Scientific Foundation of Jiangsu Province (BK20181413), and the Postgraduate Research & Practice Innovation Program of Jiangsu Province (KYCX22_1178).

Institutional Review Board Statement: Not applicable.

Informed Consent Statement: Not applicable.

Data Availability Statement: The data presented in this study are available on request from the corresponding author.

Acknowledgments: The data from Hong Kong Observatory, AVISO, NOAA-CPC and NCEP are highly appreciated. This research was supported by the National Natural Science Foundation (U1901215), the Marine Special Program of Jiangsu Province in China (JSZRHYKJ202007), the Natural Scientific Foundation of Jiangsu Province (BK20181413), and the Postgraduate Research & Practice Innovation Program of Jiangsu Province (KYCX22_1178).

Conflicts of Interest: The authors declare no conflict of interest.

References

1. Merrifield, M.A.; Merrifield, S.T.; Mitchum, G.T. An Anomalous Recent Acceleration of Global Sea Level Rise. *J. Clim.* **2009**, *22*, 5772–5781. [CrossRef]
2. Frederikse, T.; Landerer, F.; Caron, L.; Adhikari, S.; Parkes, D.; Humphrey, V.W.; Dangendorf, S.; Hogarth, P.; Zanna, L.; Cheng, L. The causes of sea-level rise since 1900. *Nature* **2020**, *584*, 393–397. [CrossRef] [PubMed]
3. Church, J.A.; White, N.J. Sea-Level Rise from the Late 19th to the Early 21st Century. *Surv. Geophys.* **2011**, *32*, 585–602. [CrossRef]
4. Masson-Delmotte, V.; Zhai, P.; Pirani, A.; Connors, S.L.; Péan, C.; Berger, S.; Caud, N.; Chen, Y.; Goldfarb, L.; Gomis, M. *IPCC Climate Change 2021: The Physical Science Basis. Contribution of Working Group I to the Sixth Assessment Report of the Intergovernmental Panel on Climate Change*; Cambridge University Press: Cambridge, UK, 2021.
5. Ericson, J.; Vorosmarty, C.; Dingman, S.; Ward, L.; Meybeck, M. Effective sea-level rise and deltas: Causes of change and human dimension implications. *Glob. Planet. Change* **2006**, *50*, 63–82. [CrossRef]
6. Duke, N.C.; Meynecke, J.O.; Dittmann, S.; Ellison, A.M.; Anger, K.; Berger, U.; Cannicci, S.; Diele, K.; Ewel, K.C.; Field, C.D. A world without mangroves? *Science* **2007**, *317*, 41–42. [CrossRef]
7. Nicholls, R.J.; Hoozemans, F.M.J.; Marchand, M. Increasing food risk and wetland losses due to global sea-level rise: Regional and global analyses. *Glob. Environ. Change* **1999**, *9*, S69–S87. [CrossRef]
8. Huang, Z.; Zong, Y.; Zhang, W. Coastal Inundation due to Sea Level Rise in the Pearl River Delta, China. *Nat. Hazards* **2004**, *33*, 247–264. [CrossRef]
9. Woodruff, J.D.; Irish, J.L.; Camargo, S.J. Coastal flooding by tropical cyclones and sea-level rise. *Nature* **2013**, *504*, 44–52. [CrossRef]
10. Stammer, D.; Cazenave, A.; Ponte, R.M.; Tamisiea, M.E. Causes for contemporary regional sea level changes. *Annu. Rev. Mar. Sci.* **2013**, *5*, 21–46. [CrossRef]
11. Cheng, X.; Qi, Y. Trends of sea level variations in the South China Sea from merged altimetry data. *Glob. Planet. Change* **2007**, *57*, 371–382. [CrossRef]
12. Fang, G.; Chen, H.; Wei, Z.; Wang, Y.; Wang, X.; Li, C. Trends and interannual variability of the South China Sea surface winds, surface height, and surface temperature in the recent decade. *J. Geophys. Res. Ocean.* **2006**, *111*, D17301. [CrossRef]
13. Peng, D.; Palanisamy, H.; Cazenave, A.; Meyssignac, B. Interannual Sea Level Variations in the South China Sea Over 1950–2009. *Mar. Geod.* **2013**, *36*, 164–182. [CrossRef]
14. Wang, L.; Li, Q.; Bi, H.; Mao, X.Z. Human impacts and changes in the coastal waters of south China. *Sci. Total Environ.* **2016**, *562*, 108–114. [CrossRef] [PubMed]
15. Ablain, M.; Legeais, J.F.; Prandi, P.; Marcos, M.; Fenoglio-Marc, L.; Dieng, H.B.; Benveniste, J.; Cazenave, A. Satellite Altimetry-Based Sea Level at Global and Regional Scales. *Surv. Geophys.* **2017**, *38*, 7–31. [CrossRef]
16. Gregory, J.M.; Church, J.A.; Boer, G.J.; Dixon, K.W.; Flato, G.M.; Jackett, D.R.; Lowe, J.A.; O'Farrell, S.P.; Roeckner, E.; Russell, G.L.; et al. Comparison of results from several AOGCMs for global and regional sea-level change 1900–2100. *Clim. Dyn.* **2001**, *18*, 225–240. [CrossRef]
17. Liu, S.; Chen, C.; Liu, K.; Mu, L.; Wang, H.; Wu, X.; Zhang, J.; Duan, X.; Gao, J. Vertical motions of tide gauge stations near the Bohai Sea and Yellow Sea. *Sci. China Earth Sci.* **2015**, *58*, 2279–2288. [CrossRef]
18. Wang, L.; Li, Q.; Mao, X.-z.; Bi, H.; Yin, P. Interannual sea level variability in the Pearl River Estuary and its response to El Niño–Southern Oscillation. *Glob. Planet. Change* **2018**, *162*, 163–174. [CrossRef]
19. Willis, J.K.; Chambers, D.P.; Nerem, R.S. Assessing the globally averaged sea level budget on seasonal to interannual timescales. *J. Geophys. Res. Ocean.* **2008**, *113*, C06015. [CrossRef]
20. Department of marine early warning and monitoring. *2020 China Sea Level Bulletin*; The Ministry of Natural Resources: Beijing, China, 2021.
21. Dangendorf, S.; Frederikse, T.; Chafik, L.; Klinck, J.M.; Ezer, T.; Hamlington, B.D. Data-driven reconstruction reveals large-scale ocean circulation control on coastal sea level. *Nat. Clim. Change* **2021**, *11*, 514–520. [CrossRef]
22. Cheng, Y.; Plag, H.-P.; Hamlington, B.D.; Xu, Q.; He, Y. Regional sea level variability in the bohai sea, yellow sea, and east china sea. *Cont. Shelf Res.* **2015**, *111*, 95–107. [CrossRef]
23. Milne, G.A.; Gehrels, W.R.; Hughes, C.W.; Tamisiea, M.E. Identifying the causes of sea-level change. *Nat. Geosci.* **2009**, *2*, 471–478. [CrossRef]
24. Cazenave, A.; Llovel, W. Contemporary sea level rise. *Annu. Rev. Mar. Sci.* **2010**, *2*, 145–173. [CrossRef] [PubMed]
25. Qu, Y.; Jevrejeva, S.; Jackson, L.P.; Moore, J.C. Coastal Sea level rise around the China Seas. *Glob. Planet. Change* **2019**, *172*, 454–463. [CrossRef]
26. He, L.; Li, G.; Li, K.; Shu, Y. Estimation of regional sea level change in the Pearl River Delta from tide gauge and satellite altimetry data. *Estuarine, Coast. Shelf Sci.* **2014**, *141*, 69–77. [CrossRef]
27. Ding, X.; Zheng, D.; Chen, Y.; Chao, J.; Li, Z. Sea level change in Hong Kong from tide gauge measurements of 1954-1999. *J. Geod.* **2001**, *74*, 683–689. [CrossRef]
28. Cabanes, C. Sea Level Rise During Past 40 Years Determined from Satellite and in Situ Observations. *Science* **2001**, *294*, 840–842. [CrossRef]
29. Willis, J.K.; Roemmich, D.; Cornuelle, B. Interannual variability in upper ocean heat content, temperature, and thermosteric expansion on global scales. *J. Geophys. Res. Ocean.* **2004**, *109*, 840–842. [CrossRef]

30. Ho, C.R.; Zheng, Q.; Soong, Y.S.; Kuo, N.J.; Hu, J.H. Seasonal variability of sea surface height in the South China Sea observed with TOPEX/Poseidon altimeter data. *J. Geophys. Res. Atmos.* **2000**, *105*, 13981–13990. [CrossRef]
31. Li, L.; Jindian, X.; Rongshuo, C. Trends of sea level rise in the South China Sea during the 1990s: An altimetry result. *Chin. Sci. Bull.* **2002**, *47*, 582–585. [CrossRef]
32. Vivier, F.; Kelly, K.A.; Harismendy, M. Causes of large-scale sea level variations in the Southern Ocean: Analyses of sea level and a barotropic model. *J. Geophys. Res. Ocean.* **2005**, *110*, C09014. [CrossRef]
33. Rong, Z.; Liu, Y.; Zong, H.; Cheng, Y. Interannual sea level variability in the South China Sea and its response to ENSO. *Glob. Planet. Change* **2007**, *55*, 257–272. [CrossRef]
34. Cheng, Y.; Hamlington, B.D.; Plag, H.-P.; Xu, Q. Influence of ENSO on the variation of annual sea level cycle in the South China Sea. *Ocean Eng.* **2016**, *126*, 343–352. [CrossRef]
35. Liu, C.; Li, X.; Wang, S.; Tang, D.; Zhu, D. Interannual variability and trends in sea surface temperature, sea surface wind, and sea level anomaly in the South China Sea. *Int. J. Remote Sens.* **2020**, *41*, 4160–4173. [CrossRef]
36. Hebrard, E.; Llovel, W.; Cazenave, A.; Rogel, P. Interannual to multidecadal variability of the mean sea level. In Proceedings of the AGU Fall Meeting Abstracts, San Francisco, CA, USA, 11–15 December 2008; pp. 33–1347.
37. Tomasicchio, G.R.; Lusito, L.; D'Alessandro, F.; Frega, F.; Francone, A.; De Bartolo, S. A direct scaling analysis for the sea level rise. *Stoch. Environ. Res. Risk Assess.* **2018**, *32*, 3397–3408. [CrossRef]
38. Huang, N.E.; Shen, Z.; Long, S.R.; Wu, M.C.; Shih, H.H.; Zheng, Q.; Yen, N.C.; Tung, C.C.; Liu, H.H. The empirical mode decomposition and the Hilbert spectrum for nonlinear and non-stationary time series analysis. *Proc. Math. Phys. Eng. Sci.* **1998**, *454*, 903–995. [CrossRef]
39. Wu, Z.; Huang, N.E. Ensemble empirical mode decomposition: A noise-assisted data analysis method. *Adv. Adapt. Data Anal.* **2011**, *1*, 1–41. [CrossRef]
40. Chen, X.; Zhang, X.; Church, J.A.; Watson, C.S.; King, M.A.; Monselesan, D.; Legresy, B.; Harig, C. The increasing rate of global mean sea-level rise during 1993–2014. *Nat. Clim. Change* **2017**, *7*, 492–495. [CrossRef]
41. Franzke, C.L.E. Nonlinear climate change. *Nat. Clim. Change* **2014**, *4*, 423–424. [CrossRef]
42. Ji, F.; Wu, Z.; Huang, J.; Chassignet, E.P. Evolution of land surface air temperature trend. *Nat. Clim. Change* **2014**, *4*, 462–466. [CrossRef]
43. Kim, Y.; Cho, K. Sea level rise around Korea: Analysis of tide gauge station data with the ensemble empirical mode decomposition method. *J. Hydro-Environ. Res.* **2016**, *11*, 138–145. [CrossRef]
44. Lan, W.H.; Kuo, C.Y.; Lin, L.C.; Kao, H.C. Annual Sea Level Amplitude Analysis over the North Pacific Ocean Coast by Ensemble Empirical Mode Decomposition Method. *Remote Sens.* **2021**, *13*, 730. [CrossRef]
45. Peng, C.K.; Havlin, S.; Stanley, H.E.; Goldberger, A.L. Quantification of scaling exponents and crossover phenomena in nonstationary heartbeat time series. *Chaos* **1995**, *5*, 82–87. [CrossRef] [PubMed]
46. Kantelhardt, J.W.; Zschiegner, S.A.; Koscielny-Bunde, E.; Bunde, A.; Stanley, H.E. Multifractal detrended fluctuation analysis of nonstationary time series. *Phys. A Stat. Mech. Its Appl.* **2002**, *316*, 87–114. [CrossRef]
47. Zhang, Q.; Zhou, Y.; Singh, V.P.; Chen, Y.D. Comparison of detrending methods for fluctuation analysis in hydrology. *J. Hydrol.* **2011**, *400*, 121–132. [CrossRef]
48. Leonarduzzi, R.F.; Torres, M.E.; Abry, P. Scaling range automated selection for wavelet leader multifractal analysis. *Signal Process.* **2014**, *105*, 243–257. [CrossRef]
49. Ihlen, E.A. Introduction to multifractal detrended fluctuation analysis in Matlab. *Front. Physiol.* **2012**, *3*, 141. [CrossRef]
50. Zhou, Y.; Leung, Y. Empirical mode decomposition and long-range correlation analysis of sunspot time series. *J. Stat. Mech. Theory Exp.* **2010**, *2010*, P12006. [CrossRef]
51. Zhang, Y.; Ge, E. Temporal scaling behavior of sea-level change in Hong Kong—Multifractal temporally weighted detrended fluctuation analysis. *Glob. Planet. Change* **2013**, *100*, 362–370. [CrossRef]
52. Ye, X.; Xu, C.-Y.; Li, X.; Zhang, Q. Investigation of the complexity of streamflow fluctuations in a large heterogeneous lake catchment in China. *Theor. Appl. Climatol.* **2017**, *132*, 751–762. [CrossRef]
53. Naren, A.; Maity, R. Modeling of local sea level rise and its future projection under climate change using regional information through EOF analysis. *Theor. Appl. Climatol.* **2017**, *134*, 1269–1285. [CrossRef]
54. McIntosh, P.C.; Church, J.A.; Miles, E.R.; Ridgway, K.; Spillman, C.M. Seasonal coastal sea level prediction using a dynamical model. *Geophys. Res. Lett.* **2015**, *42*, 6747–6753. [CrossRef]
55. Primo de Siqueira, B.V.; Paiva, A.d.M. Using neural network to improve sea level prediction along the southeastern Brazilian coast. *Ocean Model.* **2021**, *168*, 101898. [CrossRef]
56. Tur, R.; Tas, E.; Haghighi, A.T.; Mehr, A.D. Sea Level Prediction Using Machine Learning. *Water* **2021**, *13*, 3566. [CrossRef]
57. Ma, X.; Tao, Z.; Wang, Y.; Yu, H.; Wang, Y. Long short-term memory neural network for traffic speed prediction using remote microwave sensor data. *Transp. Res. Part C Emerg. Technol.* **2015**, *54*, 187–197. [CrossRef]
58. Qu, Y.; Liu, Y.; Jevrejeva, S.; Jackson, L.P. Future sea level rise along the coast of China and adjacent region under 1.5 °C and 2.0 °C global warming. *Adv. Clim. Change Res.* **2020**, *11*, 227–238. [CrossRef]
59. Dikshit, A.; Pradhan, B.; Alamri, A.M. Long lead time drought forecasting using lagged climate variables and a stacked long short-term memory model. *Sci. Total Environ.* **2021**, *755*, 142638. [CrossRef] [PubMed]

60. Tao, L.; He, X.; Li, J.; Yang, D. A multiscale long short-term memory model with attention mechanism for improving monthly precipitation prediction. *J. Hydrol.* **2021**, *602*, 126815. [CrossRef]
61. Liu, J.; Jin, B.; Wang, L.; Xu, L. Sea Surface Height Prediction With Deep Learning Based on Attention Mechanism. *IEEE Geosci. Remote Sens. Lett.* **2022**, *19*, 1–5. [CrossRef]
62. Zhao, J.; Cai, R.; Sun, W. Regional sea level changes prediction integrated with singular spectrum analysis and long-short-term memory network. *Adv. Space Res.* **2021**, *68*, 4534–4543. [CrossRef]
63. Ding, X.; Chao, J.; Zheng, D.; Chen, Y. Long-term sea-level changes in Hong Kong from tide-gauge records. *J. Coast. Res.* **2001**, *17*, 749–754.
64. Dickman, S.R. Theoretical investigation of the oceanic inverted barometer response. *J. Geophys. Res. Solid Earth* **1988**, *93*, 14941–14946. [CrossRef]
65. Zhang, X.; Zhang, G.; Qiu, L.; Zhang, B.; Sun, Y.; Gui, Z.; Zhang, Q. A Modified Multifractal Detrended Fluctuation Analysis (MFDFA) Approach for Multifractal Analysis of Precipitation in Dongting Lake Basin, China. *Water* **2019**, *11*, 891. [CrossRef]
66. Li, E.; Mu, X.; Zhao, G.; Gao, P. Multifractal Detrended Fluctuation Analysis of Streamflow in the Yellow River Basin, China. *Water* **2015**, *7*, 1670–1686. [CrossRef]
67. Zhan, C.; Liang, C.; Zhao, L.; Zhang, Y.; Cheng, L.; Jiang, S.; Xing, L. Multifractal characteristics analysis of daily reference evapotranspiration in different climate zones of China. *Phys. A Stat. Mech. Its Appl.* **2021**, *583*, 126273. [CrossRef]
68. Gómez-Gómez, J.; Carmona-Cabezas, R.; Ariza-Villaverde, A.B.; Eduardo, G.; Jiménez-Hornero, F. Multifractal detrended fluctuation analysis of temperature in Spain (1960–2019). *Phys. A Stat. Mech. Its Appl.* **2021**, *578*, 126118. [CrossRef]
69. Kantelhardt, J.W.; Koscielny-Bunde, E.; Rybski, D.; Braun, P.; Bunde, A.; Havlin, S. Long-term persistence and multifractality of precipitation and river runoff records. *J. Geophys. Res. Atmos.* **2006**, *111*, D0110. [CrossRef]
70. Hochreiter, S.; Schmidhuber, J. Long short-term memory. *Neural Comput.* **1997**, *9*, 1735–1780. [CrossRef] [PubMed]
71. Yan, J.; Mu, L.; Wang, L.; Ranjan, R.; Zomaya, A.Y. Temporal convolutional networks for the advance prediction of ENSO. *Sci. Rep.* **2020**, *10*, 1–15. [CrossRef]
72. Amiruddin, A.; Haigh, I.; Tsimplis, M.; Calafat, F.; Dangendorf, S. The seasonal cycle and variability of sea level in the S outh C hina S ea. *J. Geophys. Res. Ocean.* **2015**, *120*, 5490–5513. [CrossRef]
73. Cheng, X.; Zhao, M.; Duan, W.; Jiang, L.; Chen, J.; Yang, C.; Zhou, Y. Regime Shift of the Sea Level Trend in the South China Sea Modulated by the Tropical Pacific Decadal Variability. *Geophys. Res. Lett.* **2023**, *50*, 1–8. [CrossRef]
74. Zhang, S.; Yang, X.; Weng, H.; Zhang, T.; Tang, R.; Wang, H.; Su, J. Spatial Distribution and Trends of Wind Energy at Various Time Scales over the South China Sea. *Atmosphere* **2023**, *14*, 362. [CrossRef]
75. Hong, B.; Zhang, J. Long-Term Trends of Sea Surface Wind in the Northern South China Sea under the Background of Climate Change. *J. Mar. Sci. Eng.* **2021**, *9*, 752. [CrossRef]
76. Kim, Y.-Y.; Kim, B.-G.; Jeong, K.Y.; Lee, E.; Byun, D.-S.; Cho, Y.-K. Local Sea-Level Rise Caused by Climate Change in the Northwest Pacific Marginal Seas Using Dynamical Downscaling. *Front. Mar. Sci.* **2021**, *8*, 620570. [CrossRef]
77. Han, G.; Huang, W. Low-frequency sea-level variability in the South China Sea and its relationship to ENSO. *Theor. Appl. Climatol.* **2008**, *97*, 41–52. [CrossRef]
78. Zou, F.; Tenzer, R.; Fok, H.S.; Meng, G.; Zhao, Q. The Sea-Level Changes in Hong Kong From Tide-Gauge Records and Remote Sensing Observations Over the Last Seven Decades. *IEEE J. Sel. Top. Appl. Earth Obs. Remote Sens.* **2021**, *14*, 6777–6791. [CrossRef]
79. Xi, H.; Zhang, Z.; Lu, Y.; Li, Y. Mass sea level variation in the South China Sea from GRACE, altimetry and model and the connection with ENSO. *Adv. Space Res.* **2019**, *64*, 117–128. [CrossRef]